

The design and performance of a prototype water Cherenkov optical time-projection chamber

Eric Oberla^a, Henry J. Frisch^a

^a*Enrico Fermi Institute, University of Chicago; 5640 S. Ellis Ave., Chicago IL, 60637*

Abstract

A first experimental test of tracking relativistic charged particles by ‘drifting’ Cherenkov photons in a water-based optical time-projection chamber (OTPC) has been performed at the Fermilab Test Beam Facility. The prototype OTPC detector consists of a 77 cm long, 28 cm diameter, 40 kg cylindrical water mass instrumented with a combination of commercial 5.1×5.1 cm² micro-channel plate photo-multipliers (MCP-PMT) and 6.7×6.7 cm² mirrors. Five MCP-PMTs are installed in two columns along the OTPC cylinder in a small-angle stereo configuration. A mirror is mounted opposite each MCP-PMT on the far side of the detector cylinder, effectively doubling the photo-detection efficiency and providing a time-resolved image of the Cherenkov light on the opposing wall. Each MCP-PMT is coupled to an anode readout consisting of thirty 50Ω microstrips. A 180-channel data acquisition system digitizes the MCP-PMT signals on one end of the microstrips using the PSEC4 waveform sampling-and-digitizing chip operating at a sampling rate of 10.24 Gigasamples-per-second. The single-ended microstrip readout determines the time and position of a photon arrival at the face of the MCP-PMT by recording both the direct signal and the pulse reflected from the unterminated far end of the strip. The detector was installed on the Fermilab MCenter secondary beam-line behind a steel absorber where the primary flux is multi-GeV muons. Approximately 80 Cherenkov photons are detected for a through-going muon track in a total event duration of ~ 2 ns. By measuring the time-of-arrival and the position of individual photons at the surface of the detector to ≤ 100 ps and a few mm, respectively, we have measured a spatial resolution of ~ 15 mm for each MCP-PMT track segment, and, from linear fits over the entire track length of ~ 40 cm, an angular resolution on the track direction of ~ 60 mrad.

Keywords:

Time-of-Flight; Cherenkov light; Optical Time Projection Chamber; Microchannel Plate Photomultiplier; track reconstruction; particle detector

1. Introduction

We report the design, construction, and performance of a small prototype ‘Optical Time Projection Chamber (OTPC) consisting of 40 kg of water viewed by five Micro-channel Plate Photomultipliers (MCP-PMTs). The principle of the OTPC is that with photodetectors with adequate time and space resolution, measuring the time and position of arrival of each individual photon emitted by Cherenkov radiation from

Email address: ejo@uchicago.edu (Eric Oberla)

charged particles traversing a volume allows the measurement of the photon drift times. Given the arrival positions and the drift times, the track position and direction can be reconstructed, in analogy with reconstructing tracks from the electron drift times in a conventional gaseous or noble liquid TPC.

Due to the faster drift velocity in a medium of photons compared to that of electrons, the expected spatial resolution measured by timing will be poorer. However, the scale for the required spatial resolution for a large water neutrino detector, for example, is set by the radiation length in water, which is approximately 40 cm [1]. A resolution of less than a few cm per optical sensor may then be adequate to do event tracking for isolated or separated tracks.

The OTPC rests on three enabling technologies:

1. the use of MCP-based photodetectors with a single photo-electron transit-time resolution measured in 10's of picoseconds and a correlated position measurement with a resolution measured in mm [2, 3, 4, 5], able to cover a large surface area economically. In a conventional large water Cherenkov detector the size of the PMT precludes knowing the position of arrival to within the size of the cathode.
2. The use of microstrip anodes [6, 7], with bandwidths matched to the photodetector pulse, to cover large areas while preserving the temporal and spatial information encoded by the incident photon. The microstrips provide spatial resolution along the strip direction from the difference in pulse arrival times at the two ends, and in the transverse direction by charge sharing among strips, allowing mm resolution in two dimensions while requiring only a one-dimensional array of electronics readout channels [8].
3. The development of an economical (in quantity) low-power waveform sampling Application Specific Integrated Circuit (ASIC) capable of multiple samples on the rising edge of the fast pulse from an MCP-PMT [3, 5], and intrinsic intra-chip jitter measured in picoseconds. In this case we have developed the PSEC4 ASIC, operated at 10.24 Gigasamples-per-second, with an effective dynamic range of 10.5 bits [9].

The prototype whose design and performance is described below differs from a future large detector. In particular, a small path length allows ignoring dispersion of the photon velocities and scattering in the water. On the other hand, the much larger LAPPDTM detectors have demonstrated a gain 10-times larger than the commercial MCP-PMTs used here, with the potential for better time resolution[10, 8]. In a larger detector, measuring tracks over a longer length and with a larger photo-detection coverage would provide more constraints on the 3D event topology (including the potential for an extended and optimized use of optical mirrors).

1.1. A prototype OTPC

To demonstrate this technique, we have built a 40 kg water Cherenkov detector using a combination of commercial MCP-PMTs and optical mirrors. A concept drawing of the optical setup of one of the five MCP-PMT's of this detector is shown in Figure 1. For each planar MCP-PMT mounted on the water volume, a mirror is mounted on the opposing side creating an image of the Cherenkov light hitting the opposing wall. For a given charged particle track, the mirror adds a discrete set of reflected photons that can be time-resolved from the direct photons, thus economically doubling the photo-detection efficiency over the angular acceptance of the detector.

As the LAPPD MCP-PMTs are not yet available for use outside of a test setup [8, 11], this prototype relies on commercial MCP-PMTs that exhibit approximately the same detection resolutions, but with 1/16 the photo-active area per unit. The commercial photo-detector used is the Planacon XP85022 MCP-PMT

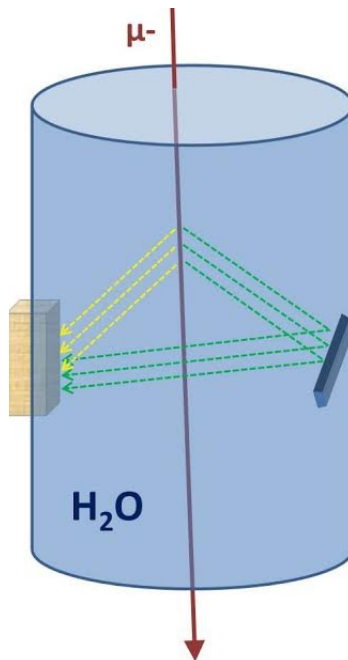


Figure 1: The concept of the prototype water-based OTPC. A charged particle emits Cherenkov light in the water volume. For each time and spatial-resolving MCP-PMT (left), a mirror is mounted on the opposing side. The mirror adds a discrete set of reflected photons (green) that arrive at the MCP-PMT after a delay due to the extra path length, and can be time-resolved from the direct photons (yellow).

device from PHOTONIS [12]. The total photo-cathode coverage in the prototype OTPC is 125 cm^2 on the surface area of 1700 cm^2 that encloses the fiducial volume.

1.2. Organization of the Paper

The OTPC prototype detector is described in §2, including the design of the optics in §2.2 and details on the photodetector modules (PM) in §3. The readout system, consisting of the fast waveform sampling digitizers of the front-end and the data-acquisition system (DAQ), is described in §4. Section 5 describes the experimental setup in the Fermilab MCenter Test Beam area, and the trigger used in the data-taking follows in §6. The reduction of the raw data to times and positions is presented in §7. Section 8 describes the response of the detector to single photons. The OTPC photo-detection efficiency and gain are derived in Sections 9.1 and 9.2. The test-beam results are shown in the final four sections, including the number of photo-electrons along the track (§10), resolving the direct and mirror-reflected Cherenkov photons and the time-projection along the beam axis (§11), the angular resolution (§12), and the spatial resolution of the reconstructed tracks (§13). The conclusions are given in §14.

2. Detector

The prototype OTPC detector is constructed from a 24 cm inner-diameter Poly-Vinyl Chloride (PVC) cylindrical pipe cut to a length of 77 cm [13]. Six 11 cm diameter ports were machined in the tube arranged in 2 columns of three ports each along the cylindrical axis, as shown in Figure 2. These columns have an azimuthal separation of 65° . The photodetector modules (PMs), described in §3, are mounted on five of

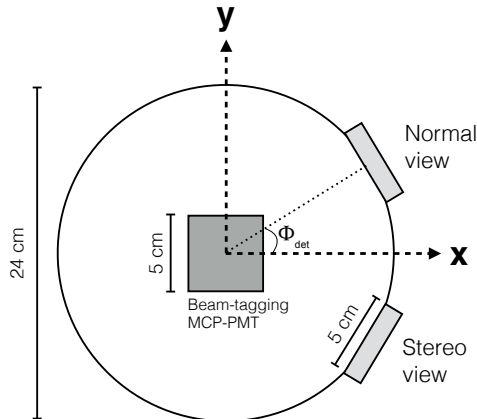


Figure 2: Rear-view scale drawing of OTPC detector showing the normal and stereo MCP-PMT mounting positions. The normal and stereo mounted PMs are symmetrical about the x-axis in the OTPC coordinate system, and separated by an azimuthal angle of $\Phi_{det} = 32.5^\circ$. The beam comes out of the page in the $+z$ direction

these ports (the 6th port was occupied by a conventional PMT used as a diagnostic trigger). The column with 3 PMs installed is denoted the ‘normal’ view and the other the ‘stereo’ view.

For each PM, a first-surface broadband optical mirror is mounted on the opposing wall facing the PM port. The 7.6 cm square mirrors are installed on the interior wall of the cylinder at an angle of 48° , denoted as θ_{mirror} in Figure 3. The remaining exposed PVC surfaces of the interior wall are coated with light absorbing paint [14].

The detector is filled with 40 L of deionized water for the target volume. Because of the detector angular acceptance, the Cherenkov light directionality, and since only the first five the ports are instrumented, the effective fiducial volume is limited to roughly the top two-thirds of the total volume, corresponding to a fiducial mass of ~ 25 kg.

2.1. Water quality

The optical quality of the water in the OTPC was measured to be notably poor, although it was not a limitation for the short photon path lengths in this detector. We found the water attenuation length by measuring 1-cm-deep samples with a dual-beam spectrophotometer [15] at various post-fill intervals, as shown in Figure 4. Compared to a pure water standard, the absolute absorbance at over the 300-500 nm range is 50 to 100 times worse. This can be attributed to several factors. One, there is no filtration system to remove particulates in the volume. Second, in the 12 hr and 60 day measurements a noticeable degradation in the near-UV part of the spectrum was observed. This is likely due to UV stabilizers in the PVC enclosure leaching into the water [16]. Data taken within the first 6 hours of a water fill have a $1/e$ attenuation length > 0.5 m at 300 nm. The longest path lengths in the OTPC, taken by the mirror-reflected photons, are approximately 0.3 m.

2.2. Detector Optics

The optical properties of the detector components in the light path, as quoted by the manufacturers [12, 14], are shown versus wavelength in Fig. 5. Despite efforts to capture as much near-UV Cherenkov light as

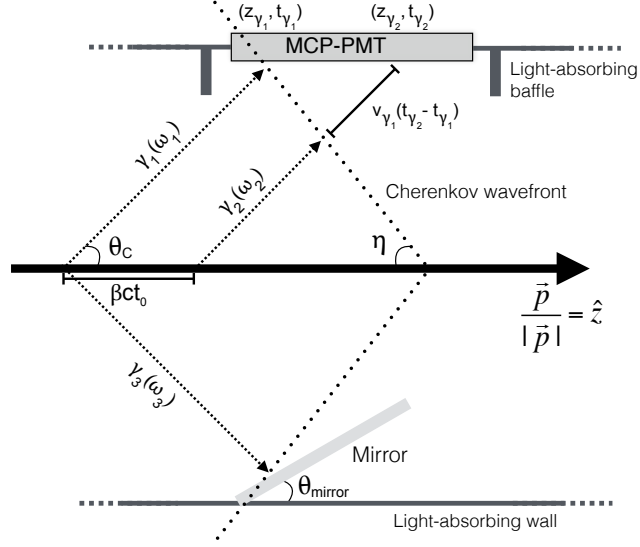


Figure 3: Two-dimensional projection of the Cherenkov light generated by a relativistic charged particle (heavy, black arrow) and the OTPC optics. The drawing shows the optical paths of three photons: γ_1 and γ_2 are directly detected, γ_3 is reflected at the mirror. The mirror is mounted at an angle, θ_{mirror} , of 48° .

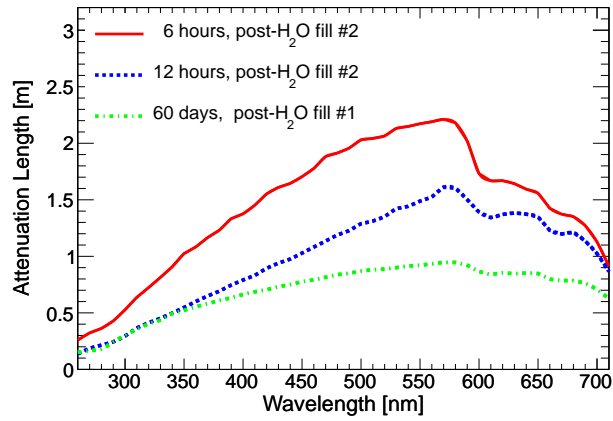


Figure 4: Calculated attenuation length of the OTPC water samples over a wavelength range of 250 to 720 nm using data obtained from dual-beam spectrophotometer measurements.

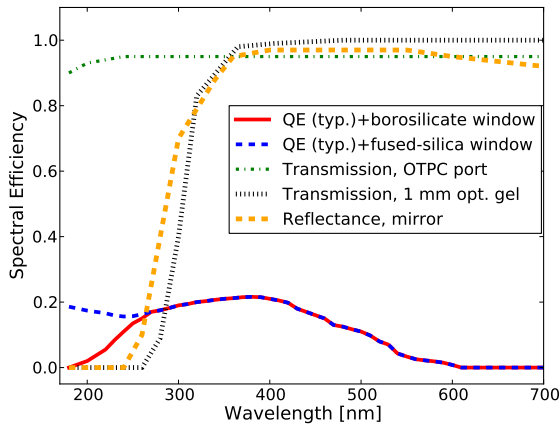


Figure 5: Optical properties of the OTPC optical components over wavelength range of 200 to 700 nm. These parameterizations are used to model the optical properties in a simulation of the detector using the Chroma toolkit [17].

possible by using fused-silica windows, we found that these wavelengths are cut off by the optical coupling gel between the window of the port and the MCP-PMT. The characteristics of the light-absorbing paint were modeled with a broadband 95% absorbance and a 5% diffuse reflectance.

With low-timing jitter and high granularity MCP-PMTs, the water chromaticity and scattering properties become important as the distance from the particle track to the photo-detector increases. The Cherenkov photons, which are generated at an angle specified by the phase velocity of the dielectric medium, propagate at the speed at which energy is transported in the dielectric: the group velocity. As shown by Jackson [18], the group velocity is expressed as

$$v_g(\omega) = \frac{c}{n_g(\omega)} = \frac{c}{n(\omega) + \omega (dn/d\omega)} \quad (1)$$

where $n(\omega)$ and $n_g(\omega)$ are the phase and group index of the medium, respectively. The group index is both greater in magnitude and more dispersive than $n(\omega)$, as shown in Figure 6a.

The spectrum of detected photons is the convolution of the OTPC spectral response and the Cherenkov spectrum [19]. A full detector simulation, which includes the OTPC geometry, water volume, and optics, was built using the Chroma toolkit [17]. A simulation of 10^4 muons with a uniform distribution of energies between 1 and 10 GeV gives a spectrum of detected photons of 370_{-50}^{+110} nm, with the spread covering about 95% of the spectrum around the mean wavelength. Over this wavelength range, $\langle n/n_g \rangle \approx 0.97$.

The relative timing errors due to chromatic dispersion of the group velocity are shown in Figure 6b. At the maximum photon drift-length in the prototype OTPC (≈ 30 cm), the expected timing error is about ± 25 ps, which is small compared to the measured single photon timing resolution of 75 ps shown in §8. Averaging over the dispersion effects, the effective photon drift-speed in the OTPC is given by the weighted average of the group velocity over the detected photon spectrum, $\langle v_{group} \rangle = 218 \text{ mm ns}^{-1}$.

2.3. Track reconstruction equations

Consider a particle traveling through the OTPC as shown in Figure 3, but further generalizing the track by allowing a polar angle, θ_i , with respect to the z-axis (see the caption of Figure 2). Two Cherenkov photons

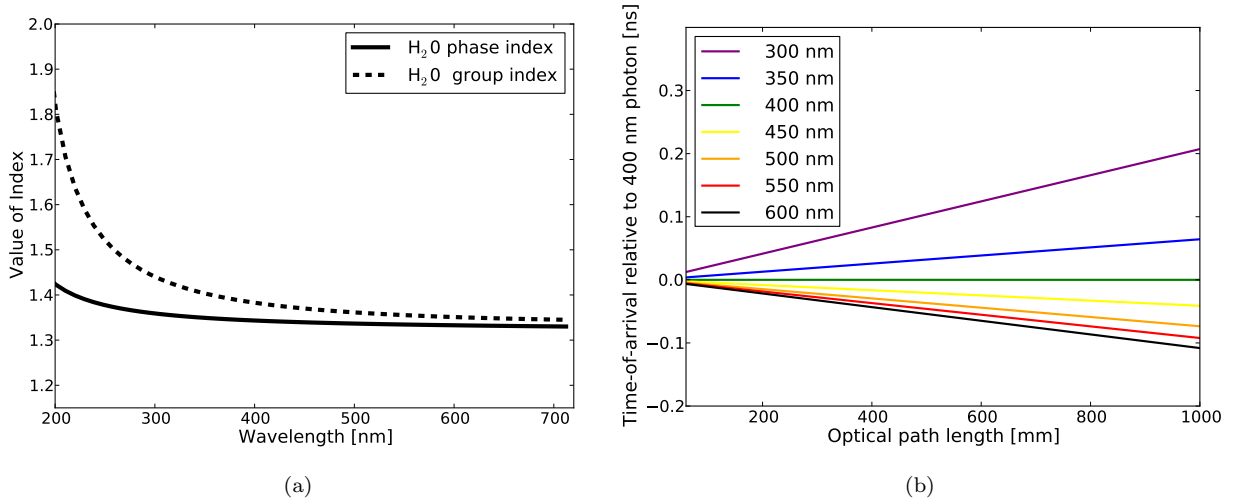


Figure 6: (a) Phase and group indices of refraction in water over the optical wavelength range. The water phase-index of refraction data were taken from [20]. (b) Timing errors due to chromatic dispersion of the group velocity, referenced to a 400 nm photon, versus optical path length.

generated along the particle path at $t = 0$ and $t = t_0$ are detected with a relative time and longitudinal position of $\Delta t_{\gamma_{21}} = t_{\gamma_2} - t_{\gamma_1}$ and $\Delta z_{\gamma_{21}} = z_{\gamma_2} - z_{\gamma_1}$. The relative timing is given by

$$\Delta t_{\gamma_{21}} = t_o + \left(\frac{L_{\gamma_2}}{v_{\gamma_2}} - \frac{L_{\gamma_1}}{v_{\gamma_1}} \right) = t_o + \frac{\Delta L_{\gamma_{21}}}{\langle v_{group} \rangle} \quad (2)$$

where $\Delta L_{\gamma_{21}}$ is the path length difference and $\langle v_{group} \rangle$ is the weighted average of the group velocity over the optical range of the detector. The experimentally measured relative times and z-positions in terms of the track variables are

$$\Delta t_{\gamma_{21}} = t_o \left(1 - \frac{\beta c}{\langle v_{group} \rangle} \tan \theta_i \right) \quad (3a)$$

$$\Delta z_{\gamma_{21}} = \beta c t_o \cos \theta_i \quad (3b)$$

A useful relation is the time-projection on the z coordinates. The projection over an infinitesimal track length is

$$\frac{dt}{dz} \approx \frac{1}{\beta c} - \frac{\tan \theta_i}{\langle v_{group} \rangle} \quad (4)$$

for small angles along a path parallel to the detector plane. The OTPC photon drift speed in Eqn. 4 is given by $\langle v_{group} \rangle$.

An additional set of reflected photons is detected at each MCP-PMT from a mirror mounted on the opposite side of the inner cylinder as shown by γ_3 in Figure 3. This is not a necessary ingredient of an OTPC, but is an effective and economical method of increasing limited photocathode coverage. Each mirror is mounted at an angle, θ_{mirror} of $90^\circ - \theta_c$. For a small range of particle angles, the mirror creates a time-delayed image of the Cherenkov light on the opposing wall at the MCP-PMT.

The discrete mirror positions provide a technique to measure the longitudinal track location across a

single MCP-PMT by using the measured time difference between the direct and mirror-reflected Cherenkov light. The displacement, r , from the OTPC center-line is given by

$$r = \frac{1}{2} (\Delta t < v_{group} > - d) \left(\frac{1}{\sin \theta_c} - \frac{< v_{group} >}{\beta c \tan(\theta_c)} \right)^{-1} \quad (5)$$

where Δt_{mirror} is the measured time difference at the MCP-PMT and d is the inner cylinder diameter. Averaging over the dispersion effects and using $\beta=1$, we insert values in Eqn. 5:

$$r = 0.737 (\Delta t < v_{group} > - d) \quad (6)$$

The scaling factor accounts for relative optical path lengths when the particle is off the OTPC center-line. For example, for tracks closer to the mirror, the reflected Cherenkov photons detected at the PM are generated along the charged particle track at a later time than the direct photons. The distance, d , from the angled mirror center-point to the photo-detector module is 18 ± 1 cm.

3. Photodetector Module

The OTPC is instrumented with five Photodetector Modules (PM), which provide the photon detection using the commercial ‘Planacon’ XP85022 MCP-PMT device from PHOTONIS [12]. These square devices have a 5×5 cm² photo-active area and an anode comprised of a 32×32 square pad array with a 1.6 mm pad pitch. The three MCP-PMTs mounted in the normal view are 25 μ m MCP-pore-size tubes with fused silica windows manufactured in 2014-15. On the stereo view are 2 MCP-PMTs; one from the same manufacturing run, and another considerably older MCP-PMT with a borosilicate window. The latter MCP-PMT exhibited lower gain and detection efficiency.

While reading out each of the Planacon’s 1024 anodes might provide the best-case granularity and pile-up rejection per channel, it presents a challenge when instrumenting a detector with many such photo-detectors. Instead, we adopt a similar microstrip readout scheme as the first-generation glass package LAPPDs [7, 6]. A thirty-two channel microstrip anode PCB board was designed such that a column of 32 anode pads is mapped to a single 50 Ω transmission line. Each microstrip line serves as both the DC return and the high fidelity signal path for $\frac{1}{32}$ of the MCP-PMT. The central 30 strips are digitized while keeping the two edge strips terminated at 50 Ω . The board-mounted photo-tube is shown in Figure 7.

The accelerated electron shower from the MCP will induce a quasi-TEM wave between the microstrip’s signal and reference plane [21]. Once created, this wave will propagate equally along both directions on the 1D microstrip. Two high-density multi-channel 50 Ω coaxial cables per microstrip array end bring these waveforms off the board [22]. The readout strategy adopted for the OTPC is to digitize the waveforms on the microstrips at only one end, leaving the multi-channel cables at the other end unterminated. Thus, the wave that initially propagates along a transmission-line microstrip toward the open end will be reflected with the same polarity back towards the digitizer for that strip, which then captures the waveforms caused by the initial pulse in both its direct and reflected manifestations (see Fig. 7 and §4).

For a single photo-electron signal, the digitizer will record two transient waveforms along the microstrip. The times of the direct and open-end reflected waves, t_1 and t_2 can be extracted from these transients, as diagrammed in Figure 7. Using the measured times we can solve for the photon longitudinal position, x ,

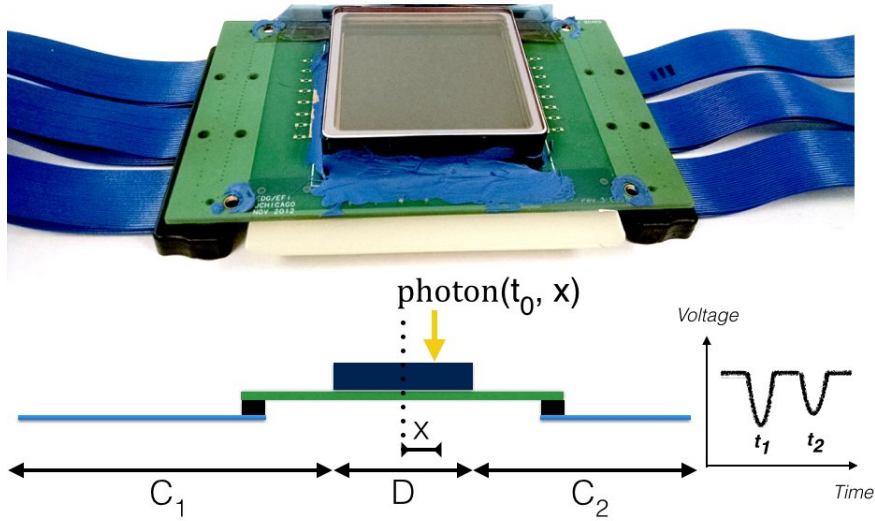


Figure 7: A PHOTONIS XP85022 Planacon MCP-PMT [12] mounted on a custom thirty-two channel, $50\ \Omega$ transmission line anode board is shown in the top photograph. The Planacon has an anode of 1024 pads in a 32×32 array over the $5 \times 5\ \text{cm}^2$ active area. These are mapped to the microstrip anode readout card in rows of 32. The bottom diagram outlines the technique for using the single-channel waveform timing to extract the incident photon position along the transmission line. The times of the direct and open-end reflected waves on the anode microstrip are denoted by t_1 and t_2 .

and time-of-arrival, t_o :

$$x = v_{prop} \frac{t_2 - t_1}{2} - \frac{D + 2C_1}{2} \quad (7a)$$

$$t_o = \frac{t_2 + t_1}{2} - \frac{1}{v_{prop}}(D + C_2 + C_1) \quad (7b)$$

where D , C_1 , and C_2 are the microstrip lengths of the MCP-PMT footprint, the reflected wave cable length, and the direct wave cable length respectively. The wave speed along the microstrip is v_{prop} , and is derived in §8.1. A 10" (25.4 cm) high density coaxial cable provides a delay for the reflected signal and an identical 6" (15.2 cm) cable connects the microstrip card to the waveform digitizer board [22].

4. Front-end data acquisition

The waveforms on the anode microstrip of each PM are digitized at 10.24 Gigasamples-per-second (GSPS) using the ACquisition and Digitization with pseC4 (ACDC) printed circuit card. This card uses 30 channels of the PSEC4 ASIC with an analog bandwidth $\geq 1\ \text{GHz}$ [9]. The signal input to the PSEC4 is AC-coupled and the on-chip signal voltage range is from 0.1-1.1 V. A pedestal voltage-level of 0.8 V is set for the OTPC data runs, allowing ample headroom for negative polarity pulses. The digitized waveforms from the PSEC4 chips are sent to an on-board field-programmable gate array (FPGA), which buffers the digital data. Serial communication and data readout to a system data acquisition card are performed over a dual low-voltage differential signaling (LVDS) link.

The ACDC card runs off a 40 MHz clock that is distributed to the five PSEC4 ASICs and FPGA using an on-board jitter-cleaning PLL chip [23]. This clock is up-converted in the PSEC4 ASIC using a voltage-

Table 1: Coarse time-base calibrations for the PSEC4 ASIC. The time-step from sample 255 to sample 0 is the ‘wraparound’ of the circular sampling buffer, and is unique.

Time step Δt_n	Value [ps]
[0,254]	96.5
255	393.3

controlled delay line (VCDL) to achieve a 10.24 GSa/s sampling rate over 256 sample cells [9]. Though an enabling and power-efficient means of garnering high sampling rates, the time-steps in a VCDL-controlled switch capacitor array are non-uniform due to process variations in the integrated circuit fabrication. Methods of calibrating of the time-base of PSEC4 and related CMOS chips are discussed in [9, 24, 25, 26].

There are two sources of error in the PSEC4 times-base: the differential non-linearity (DNL) and the integral non-linearity (INL) [9]. The DNL is the cell-to-cell time-base variation from the nominal time-step and the INL is a measure of the aggregate deviation over many sampling cells. We apply a crude calibration that considers the average INL over the PSEC4 time-base, as shown in Table 1. The time-steps between sampling cells are defined as $\Delta t_n := t_{n+1} - t_n$. With this basic calibration the sampling step is assumed to be uniform over the first 255 cells, which leaves DNL and local-INL errors uncorrected. The PSEC4 ‘wraparound’ is considered separately and has a much larger differential time-step.

5. Experimental Setup

The OTPC was installed on the beam line of the MCenter secondary beam at the Fermilab National Laboratory Test-Beam Facility [27], approximately 3 m behind a 1.09 m thick steel absorber. The absorber served as both a beam-stop for the secondary beam so that the dominant particle type seen by the OTPC was muons, and a target station and collimator to generate a tertiary beam utilized by the LArIAT experiment, to which we operated parasitically [28].

A side view of the installed OTPC is shown in Figure 8 where the upstream absorber is out of the frame. The five OTPC PM modules are mounted facing inwards on the water volume. Each of the PMs is connected to the system central cards over two Category 6 (CAT6) network cables. The system cards interface to a remotely-controlled Linux PC on an adjacent rack that also houses the beam trigger coincidence and discrimination logic. High voltage (HV) is supplied to the detector from the counting room over ~ 200 m SHV cables; the low voltage for the electronics is supplied within the enclosure. The OTPC water volume corresponds to 2.1 radiation lengths along the cylindrical axis.

The beam is delivered to the Meson Lab during the 4.2-second slow-spill at the beginning of the 60 second Fermilab accelerator complex ‘super cycle’. During the OTPC test-beam runs, a secondary beam of positive pions impinged on the MCenter target at momenta of 8, 16, or 32 GeV/c. Because the OTPC was located behind the secondary beam absorber, the particle flux was dominated by muons (85%), with a mixture of hadrons (10%), electrons (1%), and photons (4%) from punch-through and showering, as verified in a G4beamline simulation at a beam momentum of 16 GeV/c [29].

6. The Trigger

The OTPC trigger is created using two systems. The first is the beam trigger, which provides a coincidence signal of a through-going particle. Second, a level-0 (L0) trigger is made locally on each PM by

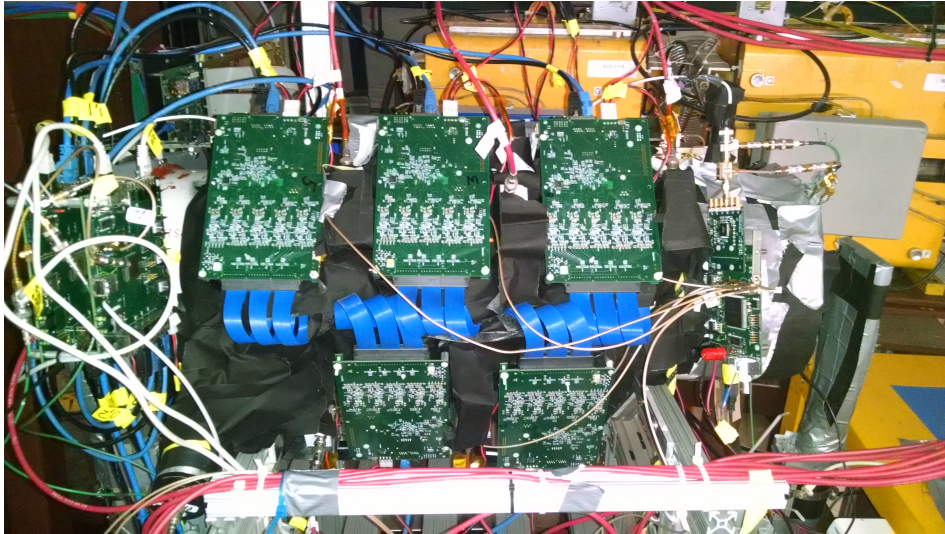


Figure 8: The prototype OTPC installed in the MC7 enclosure hall at the beam height of 208 cm. The upstream steel absorber block is out of the frame to the right. Mounted facing inwards, the five PMs connect to the system data acquisition (DAQ) cards that are mounted on the left. The DAQ system connects to a remotely-controlled laptop on an adjacent rack, which also houses the beam trigger coincidence and discrimination logic. The yellow dipole magnets on the adjacent tertiary beam-line used by the LArIAT experiment are visible in the background.

discriminating the analog signals on every channel using the PSEC4 threshold-level trigger. This two-level system is required when using the PSEC4 chip due to its relatively short analog memory. When running the PSEC4 at a sampling rate of 10.24 GSPS, the waveforms on the PSEC4 capacitor array are over-written in 25 ns intervals. The beam coincidence trigger decision requires a few hundred nanoseconds due to cable and electronic delays, which necessitates the fast L0 trigger to save these signals.

6.1. Beam trigger system

The beam trigger is a set of scintillator and Cherenkov detectors external to the OTPC water volume, as shown in Figure 9. A pair of 5×5 in² plastic scintillators mounted fore (S_1) and aft (S_2) provide good coverage over the OTPC cross-sectional area. Another pair of detectors, R_1 and R_2 , are MCP-PMTs coupled to fused-silica Cherenkov radiators that provide a prompt beam-trigger signal. R_1 is a 1×1 in² active area, single-pixel MCP-PMT mounted on the front cap of the OTPC¹. In the central region of R_1 is a small cylindrical (1 cm diameter) fused-silica radiator. R_2 is a 2×2 in² MCP-PMT that is coupled to a matching 5 mm thick square fused-silica radiator. It is mounted on the rear of the detector as also shown in Figure 2.

An additional six channels of PSEC4 electronics are implemented on the OTPC to monitor the analog signals of S_1 and S_2 , as well as to provide a threshold discriminator for the R_1 signal. This is done with a PSEC4 Evaluation Card [9], which also serves to fan-out the R_1 trigger signal to the PMs as an unbiased L0 trigger signal. The R_2 signals are read out and digitized in the same manner as the PMs, allowing spatial and time-tagging of the out-going particle, as shown in Figure 10. For each event, the digitized signal from R_1 is recorded with those of R_2 , allowing for a time-of-flight measurement (≈ 100 ps resolution).

¹ R_1 is a PHOTONIS XP85011 MCP-PMT, which has an anode structure consisting of an 8-by-8 array of pixels. The R_1 signal is made by summing the central 32 pixels through 10Ω series resistors on each pixel. R_2 is an additional PHOTONIS XP85022 MCP-PMT with an anode structure of 32-by-32 pixels, read out by the 30-microstrip anode board.

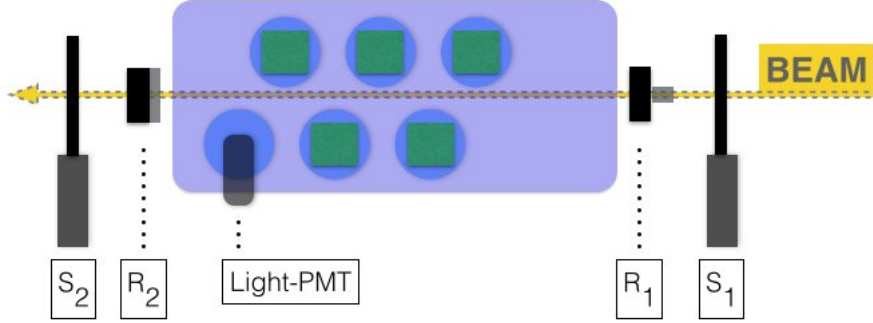


Figure 9: Diagram of the external beam-trigger (not to scale). The beam trigger coincidence can be made between four sub-detectors: the front and back scintillators+PMTs (S_1 and S_2), and the front and back fused-silica Cherenkov radiators+MCP-PMTs (R_1 and R_2). An additional diagnostic trigger is generated by a 1" PMT ('Light-PMT') mounted on the last OTPC port to observe Cherenkov light in the water volume.

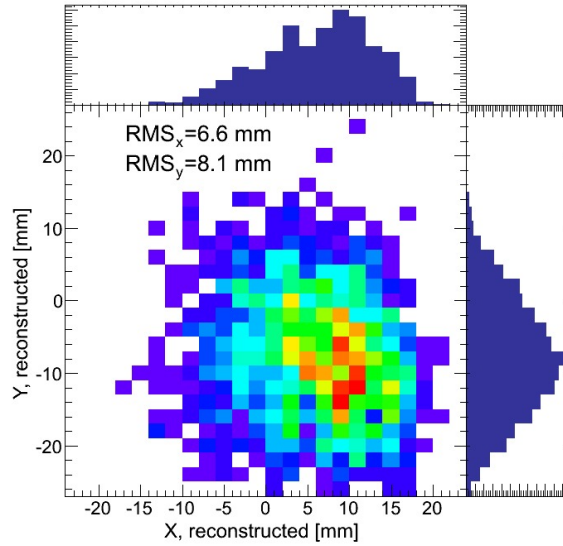


Figure 10: Reconstructed output particle position through the rear MCP-PMT+Cherenkov radiator for a 16 GeV/c dataset. This MCP-PMT is part of the beam trigger system and is denoted as R_2 in Fig. 9 in the coordinate system defined in Fig. 2. The data are histogrammed in $2 \times 2 \text{ mm}^2$ bins, where the Y direction is taken from the time difference along the anode transmission line (in the same manner as the single-photon case, §8.1) and the X position is reconstructed using the integrated-charge centroid between microstrips.

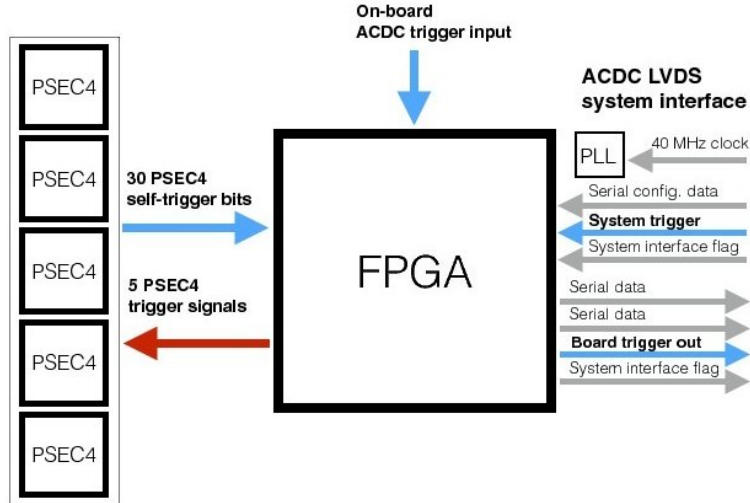


Figure 11: Diagram of the ACDC level-0 (L0) trigger and low-voltage differential signaling (LVDS) system interface. The blue lines (lighter shade) denote the ACDC trigger inputs and outputs. The L0 trigger is made as a logical combination of the 30 PSEC4 self-trigger bits and the on-board fast trigger input. In the configuration for which the L0 trigger is made in the FPGA, the five PSEC4 trigger signals (red line) are sent to the PSEC4 ASICs in order to hold their analog values. If a beam-trigger signal is received within a coincidence window of 175 ns, these values are digitized.

The beam trigger signal is made with standard NIM electronics. The signals S_1 , S_2 , and R_1 are discriminated and fed to a coincidence unit. Two configurations were used during data runs: (1) $S_1 + S_2 + R_1$, and (2) $S_1 + R_1$. Trigger configuration (1) is the default through-going particle trigger. Configuration (2) allowed the recording of particles that may scatter out, stop, or shower within the water volume. Both digital trigger signals are sent to the OTPC data acquisition system, which then sends these trigger signals to the front-end ACDC cards.

6.2. Fast level-0 trigger

The beam trigger signal is formed and returned to the OTPC electronics with a latency of approximately 130 ns due to logic and cable signal delays. The L0 trigger is implemented to hold the analog waveforms on the PSEC4 switched capacitor array if an event-of-interest is locally triggered. These waveforms are held for an adjustable length of time before either registering a beam-trigger and digitizing or, if no beam-trigger is received, releasing and re-starting the 10.24 GSPS sampling.

The L0 trigger is made within the field-programmable gate array (FPGA) on the ACDC card as outlined in Figure 11. Each of the six PSEC4 channels has a built-in threshold discriminator that asynchronously latches when an input signal crosses the threshold voltage. The signal polarity is set on the PSEC4 chip and the threshold levels are adjusted with an on-board digital-to-analog converter chip. An ACDC card has 30 such self-trigger bits that are sent to the FPGA.

The PSEC4 self-trigger bits are used in the FPGA to form the L0 trigger signal. Once the L0 trigger is made on the FPGA, the trigger signals are simultaneously sent to each of the five PSEC4 chips on the board, which then freeze the analog levels on the sampling capacitors. The round-trip L0 trigger time is 20-25 ns, which is sufficient to save the waveforms before the PSEC4 circular buffer begins to over-write.

The coincidence window between the L0- and beam-trigger signals was set to 175 ns, after which time the L0 trigger signal is released, restarting the sampling. The coincidence window allows for a small rate of accidental triggers on one or more ACDC boards, which are removed by requiring a synchronized L0 trigger time-stamp across all boards for each event.

7. Data Reduction

An OTPC event is recorded using 180 channels of 10.24 GSPS data in a time window of 25 ns. The first 150 channels contain the data from the OTPC photodetector modules (PM) and the remaining thirty channels, 150-179, contain the trigger information from the R_1 and R_2 detectors (described in §6). The digitized signal from R_1 (see Fig. 9) is saved in channel 179 and is used as a coarse zero-time reference. The events are recorded in the PSEC4 chip asynchronously to the 40 MHz system clock, which leaves the location of an event in the PSEC4 buffer undetermined. The R_1 signal time is used as a reference to find the Cherenkov photon signals in the digitized data.

The following procedures are performed on these data before analyzing an event:

1. A pedestal calibration is performed for each of the 256 sample cells in all channels [9].
2. The firmware time-stamps are checked on the front-end ACDC boards. If the time-stamps are not synchronized, the event is discarded.
3. The data on all channels are shifted in the PSEC4 buffer such that the R_1 peak-signal time is located at sample cell 90. With this shift, the hits from the Cherenkov photons are located in the first one-third of the 256 sample PSEC4 buffer.
4. A reference baseline level, created using the median value of sample cells 200-255, is subtracted from each channel.
5. A time-base is constructed from the sample-steps by applying the coarse calibration shown in Table 1. The data points that cross the wraparound region (§4) are interpolated to have an evenly spaced event time-base of 97 ps per sample.

At this point in the data reduction process, the event is aligned with respect to the R_1 trigger signal, baseline-subtracted, and referenced to a time-base. The event size is: 180 channels \times 12 bit ADC counts \times 260 time-steps over 25 ns (70 kB).

The event is further reduced by extracting the trigger information in channels 150-179, narrowing the event time-window to hold only the region of Cherenkov photon hits, and removing below-threshold channels as shown in Figure 12 [30]. After the data reduction, the event comprises the following trigger information: particle output x-position, particle output y-position, time-of-flight, R_1 trigger time, R_2 trigger time, R_1 total charge, R_2 total charge, and the number of distinct hits in R_2 . The reduced size of the event time-stream data is: number of OTPC channels above threshold (≤ 150) \times 12 bit ADC counts \times 110 time-steps over 10.67 ns (number of channels \times 0.17 kB).

7.1. Extracting the photon time-of-arrival

For each detected photon, we measure its 2D spatial position on the OTPC cylinder (z_{det} , ϕ_{det}) and its time-of-arrival, t_{det} . By projecting the measured photon arrival times on the two spatial coordinates we can reconstruct the charged particle track in 3D. We take the detected photon azimuth angle, ϕ_{det} , to be the PM location about the OTPC cylinder and its z-position, z_{det} , as the microstrip position along the OTPC

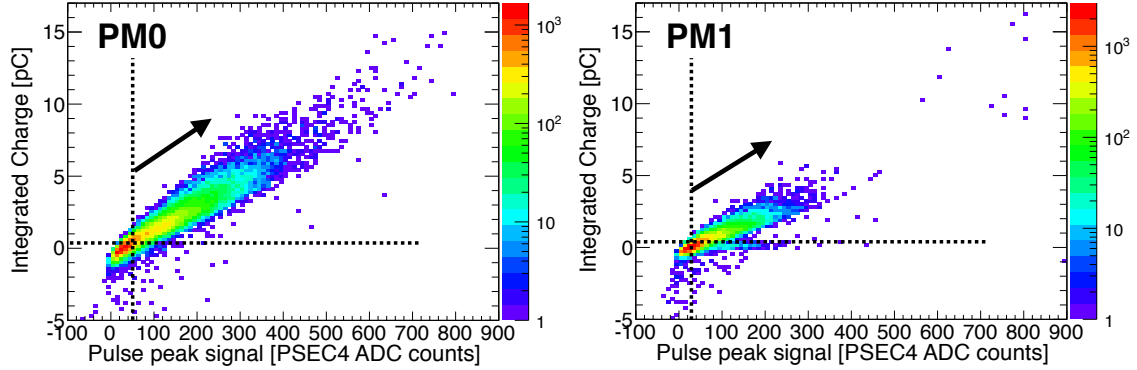


Figure 12: Correlation plots of integrated charge vs. pulse peak signal for PMs 0 and 1. Channels with waveforms above a minimum integrated charge and ADC count threshold, shown as dashed lines, are saved and further processed to measure the photon time-of-arrival.

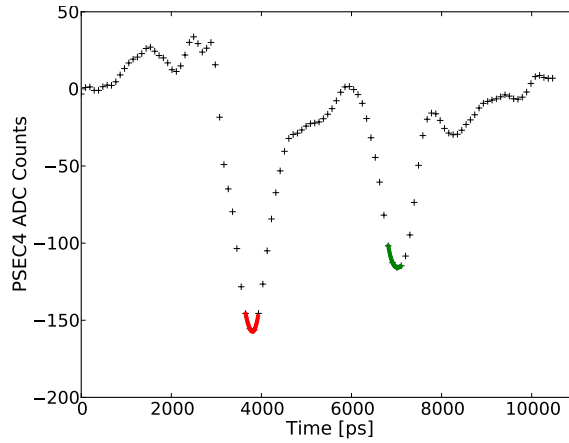


Figure 13: OTPC digitized waveform from a Cherenkov photon. A single photo-electron waveform is shown with the peak-interpolation time-extraction method. The interpolated peak-signal regions on the waveform are shown in red (green), which represent the direct (anode-reflected) pulses.

longitudinal axis. There are 2 discrete ϕ_{det} angles and 150 discrete z_{det} positions. This section describes how we extract the time-of-arrival for each photon from the digitized waveforms.

We found the most robust algorithm is to interpolate the PSEC4 waveform in a small region around the peak. A window of 4 time-steps (97 ps each) is interpolated with a cubic spline on a 9.7 ps grid and the pulse time is taken from the peak of the interpolated region. An example of an OTPC channel hit by a Cherenkov photon is shown in Figure 13.

For an event, the output of the peak-interpolation algorithm is a set of times ($[t_{1a}, \dots], [t_{2a}, \dots]$) from the direct and anode-reflected pulses. To get the photon hit time, we apply Eqn. 7b and require causality using Eqn. 7a. That is, the time difference between the direct and anode-reflected pulse should be located on the microstrip line within the 5 cm length of the MCP-PMT. The causality requirement is that $t_{2a} - t_{1a} \in [3.1, 3.9]$ ns after solving Eqn. 7a for the cable lengths in the PM.

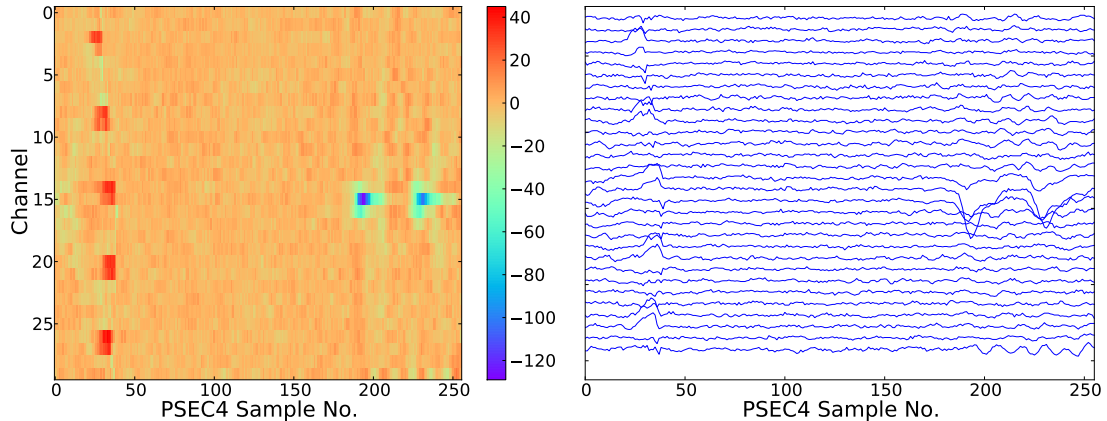


Figure 14: A single photo-electron recorded by the PM using a pulsed laser. The left panel shows the ACDC channel vs. PSEC4 sample number with the color indicative of the digitized value in PSEC4 ADC counts. The corresponding PSEC4 waveforms are shown on the right, in which the two peaks in the waveform are the direct and reflected pulses on the anode microstrip.

8. Single photo-electron response

A laser test-stand was built to characterize the single photo-electron response of the PMs. A 405 nm PiLas laser was used in pulsed mode, which can achieve pulse widths of 33 ps FWHM [31].

8.1. Single-photon

In the single photon mode, an iris is placed on the free-space output of the PiLas optical head, which picks off a 1 mm diameter portion of the beam. The iris is placed a few mm off the incident beam axis in order to produce an attenuation of approximately 50%. Following the iris is a neutral density filter (Transmittance = 10^{-5}) to attenuate the beam to the single-photon level. About 5% of the events recorded in the single-photon test setup have a laser-correlated signal.

Figure 14 shows the PM response to a single photo-electron. Typical signals are on the order of 100 PSEC4-ADC counts (~ 25 mV) for the first pulse and somewhat less for the time-lagged pulse due to the additional resistive attenuation. There is a 20 dB pre-amp board on the ACDC input so the unconditioned single photo-electron MCP-PMT signals are typically between ~ 2 -5 mV². An approximately synchronous line in many channels near the beginning of the recording window is also visible in the figure. This is the time at which the PSEC4 chips are triggered.

The single photo-electron position resolution is obtained by scanning the laser beam on the active area of the PMs both parallel and transverse to the microstrip direction. Results from a scan along the microstrip direction are shown in Figure 15. Four data points were taken at a spatial separation of 4.5 mm with a time-difference resolution of ~ 35 ps measured for all laser positions. This is the inherent electronics timing resolution for the single photo-electron pulses digitized using one channel of the PSEC4 chip, with the basic (not complete) time-base calibration described in §4.

²Measurements with the LAPPD MCPs have demonstrated gains $\geq 10^7$, which give single photo-electron signals ten-times as large into the same 50 Ω anode [8].

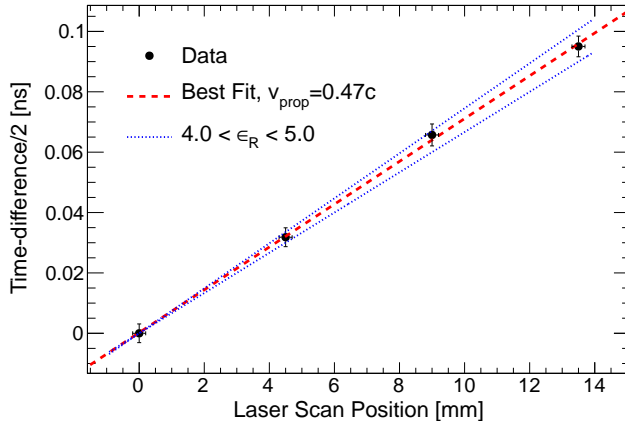


Figure 15: Single photo-electron laser scan to measure the propagation velocity along the microstrip line. The vertical error bars are the 3σ standard error on the time-difference measurement (the single event statistical error on the time-difference is ≤ 35 ps for all laser positions). The data agree with the expected velocity given the typical dielectric permittivity of an FR4 printed-circuit board substrate ($\epsilon = 4.3 \pm 0.2$).

Figure 15 shows the time difference along the microstrip vs. the laser beam position, from which the signal propagation velocity, v_{prop} , in Eqn. 7 along the microstrip to be calculated. The best fit v_{prop} is found to be $0.47 \pm 0.02 c$.

8.2. Multi-photon

A similar test-stand setup is employed to measure the relative timing between single photons within the same laser pulse. In this setting, the iris is re-aligned with the laser beam axis, and a 10 mm focal length convex lens is put in the laser path. The MCP-PMT sits 30 cm behind the lens, which projects an elliptical laser beam spot over the MCP-PMT active area. The same neutral density filter is installed after the lens to attenuate to an average of a few photons per pulse.

Events are analyzed that have two recorded photo-electrons, in which the signals are clearly separated between channels above and below the MCP-PMT center-line. The relative timing between photons is shown in Figure 16. A tail is seen in the distribution, which is likely caused by optical reflections in the test setup that are recorded late. The core resolution is shown to be 105 ps, which corresponds to a single photo-electron PM resolution of 75 ps.

From these measurements, we conclude that the $1\text{-}\sigma$ single photo-electron time-of-arrival and space statistical errors are $(\sigma_t, \sigma_x, \sigma_y) = (75 \text{ ps}, 2 \text{ mm}, 3 \text{ mm})$. The σ_x resolution is taken from the microstrip pitch on the anode board.

9. Photo-detection properties

The data presented are taken from 16 GeV/c secondary beam runs in which the optical water quality was at or above the 6-hour curve in Figure 4 and were taken using the through-going particle trigger (the beam-trigger configuration 1 as described in §6.1).

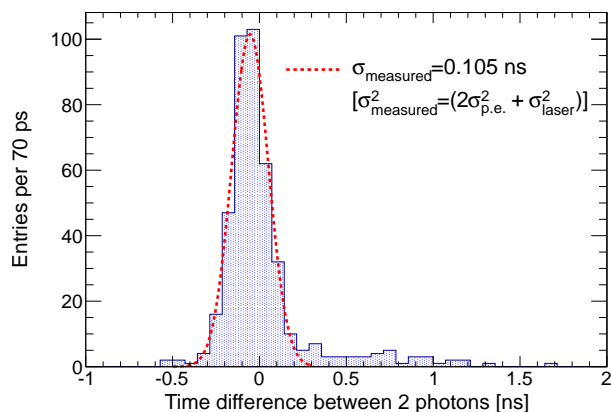


Figure 16: Relative timing measurement between 2 photons on the PM. The underlying single photo-electron electronics + MCP-PMT timing resolution for this measurement is 75 picoseconds.

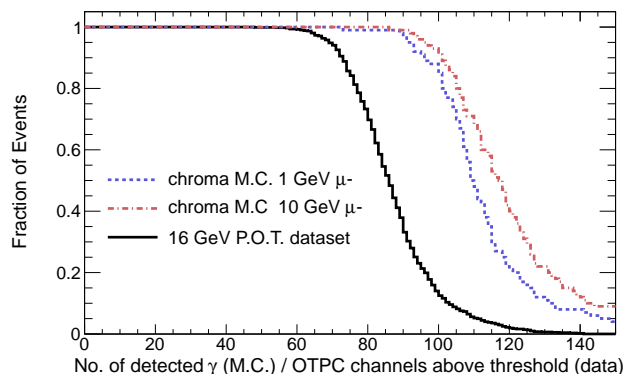


Figure 17: Fraction of events in which the number of OTPC channels is above a defined single photo-electron threshold versus the number of channels required.

9.1. Photo-detection efficiency

The number of channels that passed the signal thresholds over the 1686 event dataset is shown in Figure 17. Roughly 50% of the events have 80 or more channels above threshold per event. This is not a direct indication of the number of individual photons detected per event, but should be a decent proxy. Effects not included are over-estimation due to charge-sharing between channels and under-estimation from channels that may have two or more photon hits. From Poisson statistics, we estimate that 8% of strips will have more than one detected photon.

A comparison between data and the expectation from simulation shows a 70-80% detection efficiency compared to the Monte Carlo. Table 2 presents the sources and estimated detection losses that contribute to the observed photo-detection efficiency.

Table 2: Estimation of photo-detection inefficiencies compared to the detector Monte Carlo as shown in Fig. 17.

Source	Estimated effect	Explanation
PM baffle	$6 \pm 3\%$ loss of direct Cherenkov light	PMs 0, 2, 3, and 4 show a smaller occupancy per event in the first several channels suggesting that the PM baffle (drawn in Fig. 3) is intercepting some of the direct Cherenkov photons
Reflection losses	$10 \pm 5\%$ loss of direct Cherenkov light	Additional losses of the direct Cherenkov light due to areas of poor optical coupling at the fused-silica port window and MCP-PMT interface. For any air gaps in this interface, the critical angle for total internal reflection is $\sim 43^\circ$.
PM 1	$5 \pm 3\%$ total loss	The detector Monte Carlo did not consider variations in the detection capabilities of the 5 MCP-PMTs. PM 1 has a notably lower efficiency than the other 4 PMs.
Bad channels	$3 \pm 1\%$ total loss	Five channels in the OTPC DAQ were cut from the experimental datasets due to poor coupling. The detector Monte Carlo did not include the removal of these channels.

9.2. Single photo-electron gain

The gain per channel is shown in Figure 18, which is the multiplicative gain of the MCP-PMT, the 20 dB pre-amplifier board, and any relative gains between channels in the PSEC4 ASIC³. This is measured by taking the median integrated charge for signals above threshold over the dataset. Error bars are taken to be the RMS of the integrated charge distribution per channel. MCP-PMT gains of about 10^6 are found for PMs 0 and 2-4, who are measured to be about twice the gain of PM 1. The gain on each channel is used to calibrate the number of detected photo-electrons per event.

10. Photo-electrons along the track

Four raw time-projected events are shown in Figure 19. The PSEC4 time-step is plotted versus the OTPC channel, which is divided into 5 sub-panels representing each PM. Each sub-panel is auto-scaled with the color value indicative of the signal amplitude in PSEC4 ADC counts. The beam direction is from left-to-right. The two time-separated pulses for every signal channel are the direct and anode-reflected waveforms. These data are reduced up to step 4 in §7.

Events (a) and (b) in Fig. 19 are from the 16 GeV/c data that were recorded using the through-going trigger configuration. Events (c) and (d) are from the 8 GeV/c data, which were recorded using trigger configuration 2. These two tracks left no signal in R_2 , implying that these particles interacted in the volume, or else somehow missed the back trigger detector.

By applying the gain calibration described in §9.2, we can measure the effective number of photo-electrons along the track. Figure 20 shows the number of detected photons along the OTPC z-axis for the events

³Since a full voltage calibration was not performed on these data, there exist small gain differences between PSEC4 channels due to their relative transfer functions from input voltage to output ADC counts. The vast majority of signals are small (<10% of the PSEC4 voltage range [9]), so this is not a large effect.

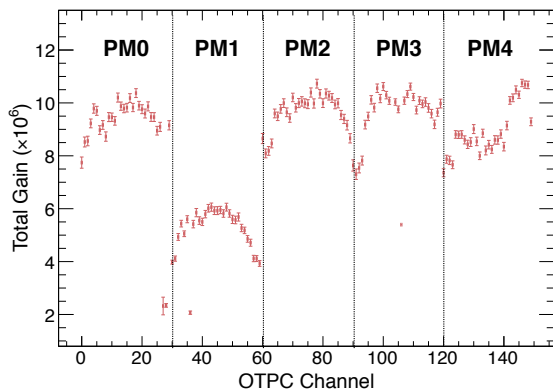


Figure 18: The OTPC per-channel gain. PM 0, 2, and 4 constitute the OTPC normal view; PM 1 and 3 are in the stereo view. The gain factor on each channel is comprised of three factors: the MCP-PMT \times electronics pre-amp gain \times variations in the PSEC4 count-to-voltage transfer function.

in Fig. 19. Event (a) has a roughly uniform number of photo-electrons along the ~ 40 cm extent of the photo-detection coverage. Event (b) shows an increase in the detected photons in the last one-third of the track, possibly due to the creation of a δ -ray along the track. Events (c) and (d) are distinct in that they exhibit a large localized peak in the number of detected photons ($>10^2$ photons per \sim cm), suggesting that these events may have an EM showering component. Event (c) could also be explained by an wide-angled muon track that exited the OTPC volume at PM 0.

10.1. Comparison of datasets

A comparison of the number of detected photons per event for datasets collected using the two trigger configurations, at different secondary beam momenta, and at varying optical water qualities is shown in Figure 21. The datasets that were acquired using the through-going trigger ($S_1+R_1+S_2$, configuration 1) have a well-defined distribution of detected photons per event, which corresponds to the predominate flux of multi-GeV muons that satisfy this trigger condition. Datasets acquired using the second trigger configuration (S_1+R_1) did not require a through-going particle. Though having a different trigger, the majority of S_1+R_1 events do pass through the OTPC and have a number of detected photons consistent with the through-going trigger. There are also several events with a large spread in the detected number of photons that are not seen in the through-going triggered events.

Figure 21a compares 8 GeV/c datasets that were recorded using different trigger configurations (Datasets 1 and 2). Dataset 1 used the through-going trigger configuration. The number of photons per event in the dataset 1 is 79 ± 20 at 1σ from a normal fit to the distribution. The second 8 GeV/c dataset, triggered in the second configuration (S_1+R_1), has an expected number of photons of 74 ± 25 with a fit over the same range. The slight difference in the mean may be attributed to the poorer water quality in the second dataset. Dataset 2 has a number of events with fewer than ~ 30 detected photons that are not observed in the through-going trigger dataset.

A similar comparison is made between a data collected at 16 GeV/c (Dataset 3) and 32 GeV/c (Dataset 4) in Fig 21b. Dataset 3 was recorded using the through-going trigger. The number of photons per event in dataset 3 is 79 ± 18 from a normal distribution fit, which corresponds to the photo-detection efficiency

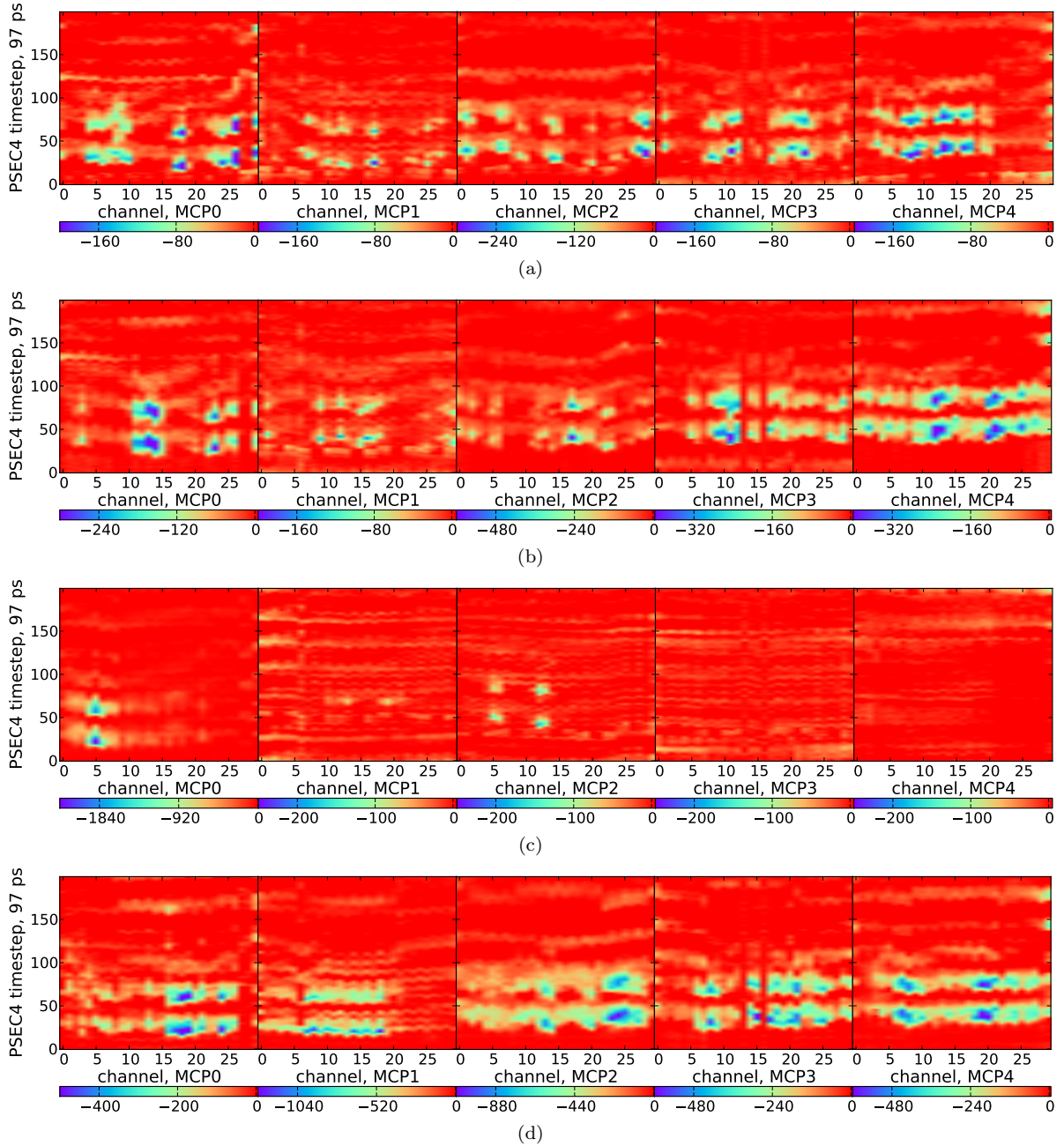


Figure 19: Raw OTPC events: time-step (97 ps per bin) vs. OTPC channel. The 5 panels in each event are the individual OTPC PMs. PMs 0, 2, and 4 constitute the OTPC normal view, PMs 1 and 3 are in the stereo view. Each panel is scaled to the maximum signal value with the color value indicative of the signal amplitude in PSEC4 ADC counts. (a) Typical through-going event that is representative of most recorded events. (b) Through-going event, in which the number of detected photons increases near the right side. (c) Track with a large number of photons over a short extent. (d) Large signal amplitude along entire track, peaking in the 2nd panel. Events (c) and (d) were recorded using trigger configuration 2 (§6.1). Events (a) and (b) were recorded using configuration 1, the through-going trigger mode.

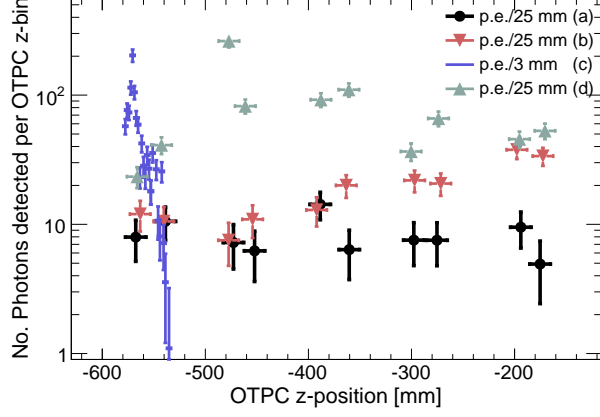


Figure 20: The number of photons detected along the OTPC z-axis, per z-bin defined by the horizontal error bars, for events presented in Fig. 19. The gain calibrations shown in §9.2 were used to convert the waveform integrated charge to a number of photo-electrons (p.e.). Events a, b, and d show the number of p.e.'s per 2.5 cm interval along the OTPC z-axis. Event c shows the number of p.e.'s per 3 mm.

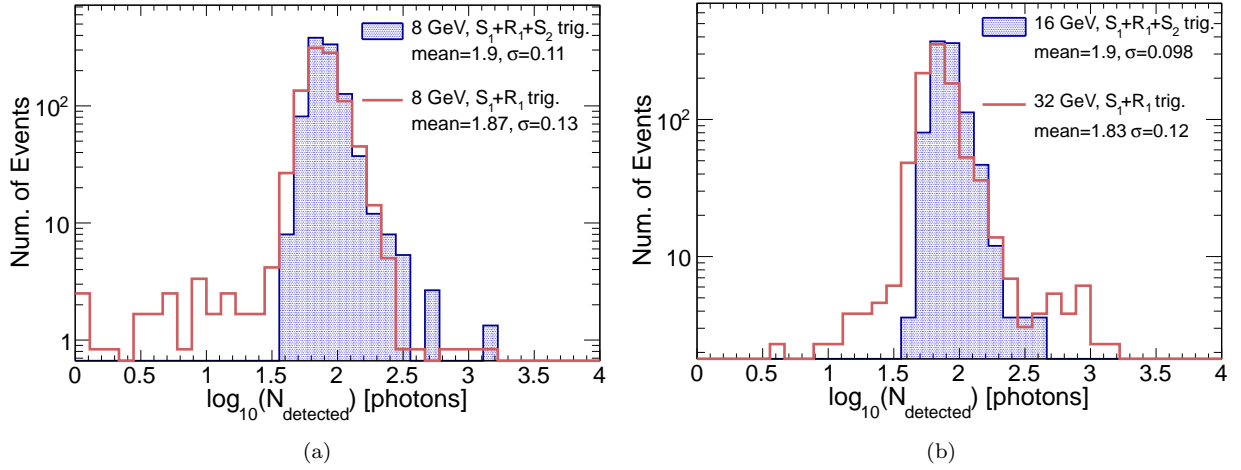


Figure 21: Dataset comparisons of the number of detected photons per event. (a) The number of photons detected per event in the 8 GeV/c datasets are compared. The data recorded using the S_1+R_1 trigger had poorer optical water quality given by the 60-day curve in Fig. 4. The through-going triggered dataset was taken with optical water quality at or better than the 6-hr curve. (b) The number of photons detected per event in 16 and 32 GeV/c datasets are compared. The 16 GeV/c data were recorded using the through-going trigger. The 32 GeV/c data were recorded using the S_1+R_1 trigger and with poorer optical water quality.

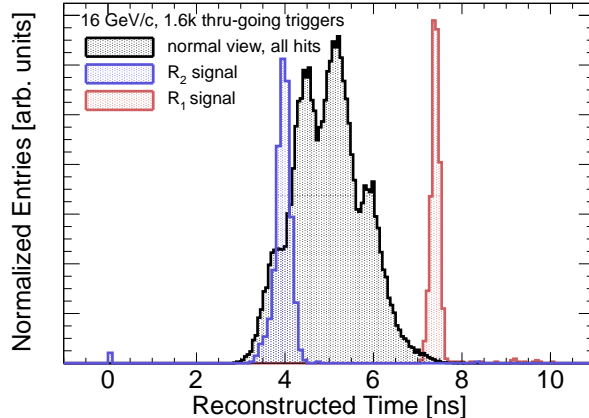


Figure 22: The times of the data and trigger signals from the reduced 16 GeV/c dataset. The reconstructed times of the detected Cherenkov photons (from the normal-view) are shown by the black histogram. The ‘fast’ trigger signals, R_1 and R_2 are shown in the red and blue, respectively. Each event is aligned with respect to the R_1 time. The time of R_1 is measured later than the R_2 signal due to cable delays.

measurement in Figure 17. Dataset 1 has a core expectation of 67 ± 22 , but a larger overall variance from events that are unique to the $S_1 + R_1$ trigger configuration. The downshift in the normal distribution between datasets may again be due to the poorer OTPC water quality when acquiring dataset 1.

11. The time-projection

In this and the following sections we use 1230 events from a secondary beam momentum of 16 GeV/c dataset, which were triggered on through-going tracks at the best measured water quality.

We now add the time dimension of the detected photons, as extracted from the waveforms in §7.1, to the data analysis. Figure 22 shows the measured time structure of the events, in which the times-of-arrival of the Cherenkov photons on the OTPC normal view are plotted with the measured times of the beam trigger signals, R_1 and R_2 . The time structure seen in the Cherenkov photon data is due to the three discrete PM locations in the OTPC normal view.

11.1. Resolving the direct and mirror-reflected Cherenkov photons

As shown in Equation 4, the particle’s time-projection along the longitudinal axis has two components: one from the particle’s velocity and the other from its angle with respect to the OTPC z-axis. For through-going multi-GeV muons, we can assume the particle’s velocity is constant along the OTPC with $\beta=1$. We introduce a rotated time basis, t' , which nulls out the velocity term in Eqn. 4

$$t'_i = t_i - \frac{z_i}{c} \quad (8a)$$

$$\frac{dt'}{dz} = \frac{dt}{dz} - \frac{1}{c} = \frac{\tan \theta}{\langle v_{group} \rangle} \quad (8b)$$

where t_i and z_i are the measured individual photon times and z-positions. As defined in §2.2, $\langle v_{group} \rangle$ is the weighted average of the group velocity dispersion over the optical efficiency range of the detector. In the t' basis, the time-projection along the OTPC z-axis is a measure of the particle angle.

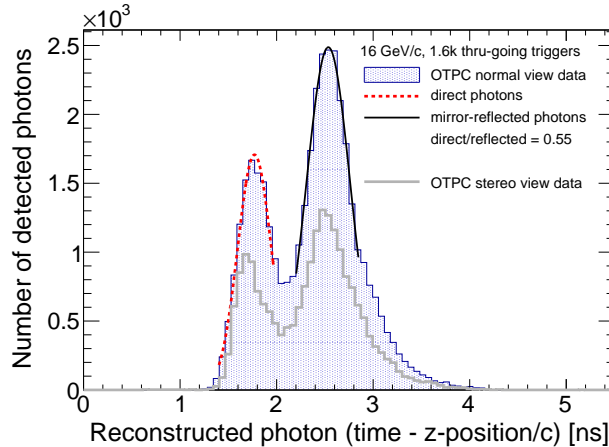


Figure 23: Histogram of the inclusive dataset of detected photons in a rotated time basis: $t'_i = t_i - z_i/c$. This removes the contribution to the time-projection along the z-axis due to the particle's velocity (assuming $\beta=1$). The direct and mirror-reflected Cherenkov photons are distinctly visible and separated by 770 ps, as taken from the fit parameters.

Figure 23 shows the distribution of the measured photon times in terms of their rotated time, t'_i . The R_2 trigger time for each track serves as a fine time-alignment between events. As expected, the t' distribution is bi-modal with peaks corresponding to the direct and mirror-reflected photons. A distinct separation of 770 ps is observed, which is consistent with the mean path length difference between the direct and reflected photons divided by the photon drift velocity, $\langle v_{group} \rangle$. The path length difference equal to the detector diameter, 18 ± 1 cm (§2.3), corresponds to an expected time difference between the direct and mirror-reflected photons of 830 ± 50 ps.

Figure 23 also shows a larger number of mirror-reflected photons than direct photons. Using the relative areas from the Gaussian fits to the distributions, we measure fewer direct than reflected photons by a factor of 0.55 in the normal view data. This was unexpected; the detector Monte Carlo predicts approximately equal numbers of each for small-angle tracks. The relative deficit of direct photons is most likely due to reflections of the direct light at the fused-silica OTPC port and MCP-PMT interface as discussed in Table 2. It is also likely that there is a small percentage of scattered photons in the data; these would arrive later than the direct photons and may be included in the mirror-reflected distribution and also cause the observed tail in the t' timing distribution after 3 ns.

11.2. An example event

Figure 24a shows the time-projection on the z-axis for the raw event shown in Fig. 19a. In this event, 73 individual photons were resolved in both time and space. Figure 24 shows their measured times, t_i , projected versus their detected positions, z_i . The photons detected in the normal and stereo views are denoted by black and red data-points, respectively. Figure 25 is a histogram of the rotated times, t'_i , of this event. The peaks in the histogram are from the measured arrival-times of the direct and mirror-reflected photons.

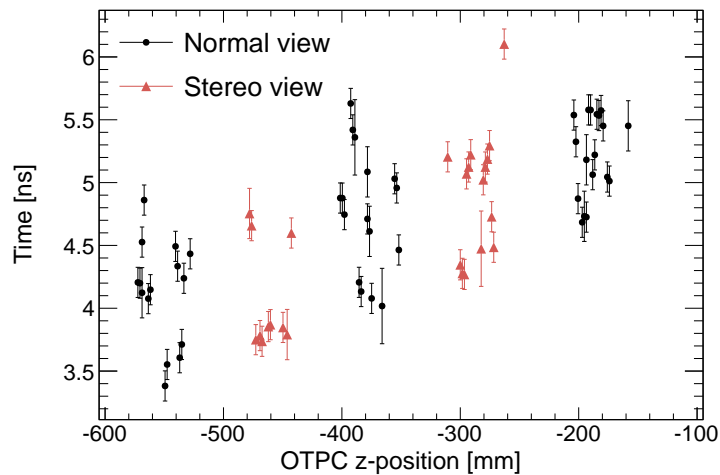


Figure 24: The time-projection along the beam axis for a single event. The time projection along the z-axis is shown for the event shown in Figure 19a using 73 individually resolved Cherenkov photons.

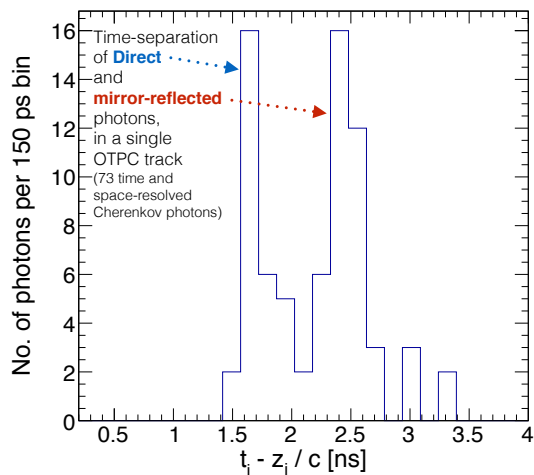


Figure 25: Histogram of the detected photon times from the event in Fig. 24, plotted in the rotated basis introduced in Fig. 23. The separated peaks in the time distribution are from the direct and mirror-reflected Cherenkov photons.

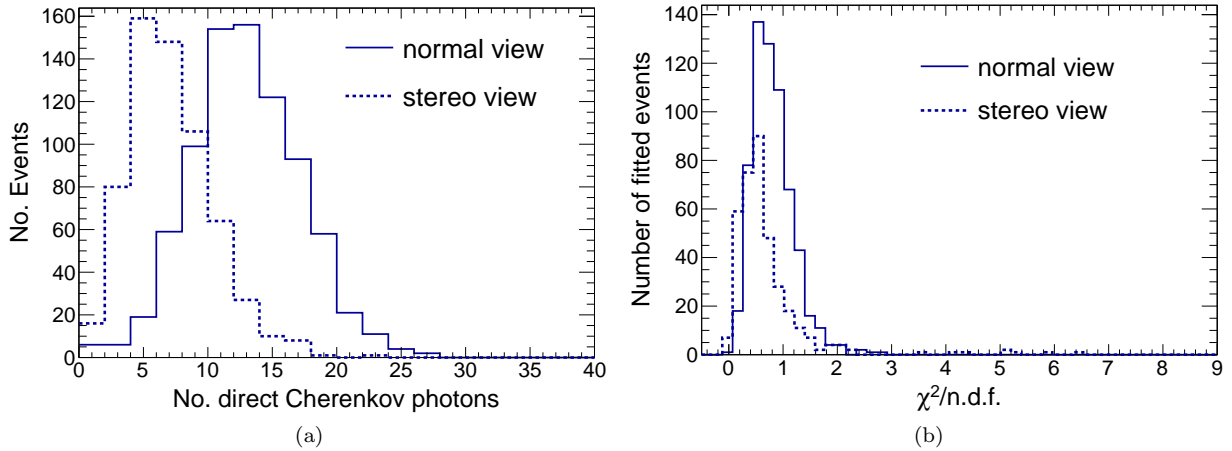


Figure 26: (a) Number of direct Cherenkov photons per event. The direct and mirror-reflected photons are separated by applying a time-cut to the data presented in Fig. 23. (b) Goodness of fit as given by the χ^2 per number of degrees of freedom (n.d.f.). Events from (a) with more than 8 normal-view and more than 4 stereo-view direct photons are used in the fit.

12. Angular resolution

The direct Cherenkov photons can be used to measure the particle angle with respect to the OTPC z -axis as shown in Eqn. 8. The most straightforward method of extracting this angle is to assume a linear track over the extent of the OTPC photodetector coverage. The slope of the linear fit, multiplied by the weighted average of the group velocity ($\langle v_{group} \rangle$), is the tangent of the track angle.

It is possible to separate the direct and mirror-reflected photons when the data are in the rotated time basis, t' , as shown in Figure 23. A normal view time-cut of <1.95 ns and a stereo view time-cut of <1.90 ns were used on the data to isolate the direct photons. The number of direct Cherenkov photons per event is shown in Figure 26a. The sample fitted consists of 522 events with more than 8 normal-view and more than 4 stereo-view direct photons are fit, requiring that each PM has at least two direct photons. Separate linear fits to the direct stereo and normal view photons are performed. The fits are reasonable, as shown by the distributions of χ^2 per degree of freedom in Figure 26b.

The returned slopes from the fits, $\frac{dt'}{dz}$, are multiplied by $\langle v_{group} \rangle = (c/1.38)$ and histogrammed in Figure 27. Linear fits to the photons in the direct normal-view yield an angle relative to the nominal beam axis over all the fitted tracks of 73 ± 60 mrad at 1σ resolution. The stereo view shows a measurement of -20 ± 121 mrad. The stereo view measurement has a larger error that is most likely due to its smaller z -coverage than the normal view, which gives it a smaller lever arm on the angular measurement. The normal view has 3 equally spaced PMs over a z -range of ~ 40 cm, but the stereo view has 2 PMs covering a z -range of only 20 cm.

A study of the angular resolution versus the number of direct Cherenkov photons in the linear fit is shown in Figure 28. As a higher minimum number of photons is required in the fit, the resolution is improved. Ninety-nine events in the dataset have more than 17 discrete normal view photons from the direct Cherenkov light. Fitting only these events results in a 1σ resolution of 48 mrad.

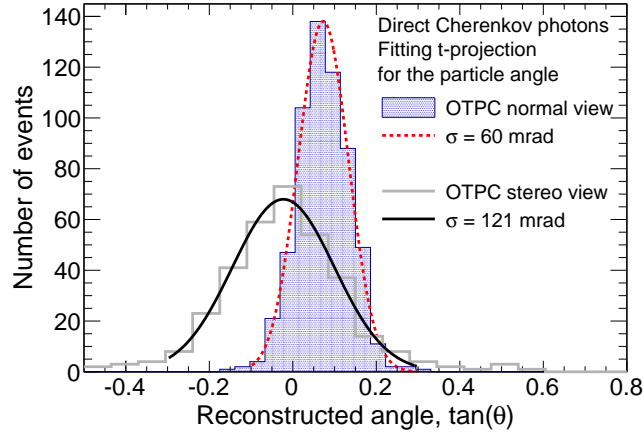


Figure 27: Measured angle of tracks along the z-axis as seen by the stereo and normal views. The direct Cherenkov light is fit with a straight line for events with more than 8 direct normal-view photons. In the stereo view, at least 4 photons are required to fit the angle. The measured angle distributions are: 73 ± 60 mrad for the normal view, -20 ± 121 mrad in the stereo view. Fits that have a $\chi^2/\text{n.d.f}$ greater than 3, as shown in Fig. 26b, were not included in this measurement.

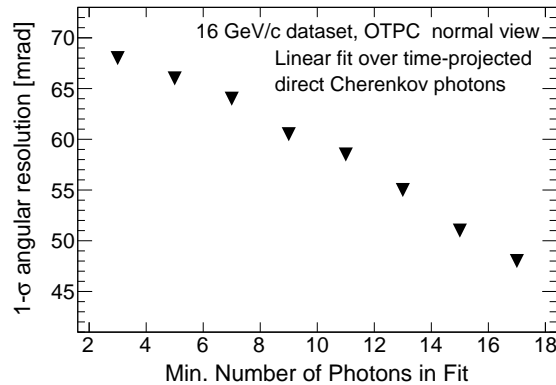


Figure 28: The 1σ angular resolution as a function of the minimum number of direct normal view photons included in the fit. The measurement in Fig. 27 is shown by the data-point with a minimum of 9 photons. An angular resolution of 48 mrad is achieved when using only events with greater than 17 direct photons in the normal view (99 events in the 16 GeV/c dataset).

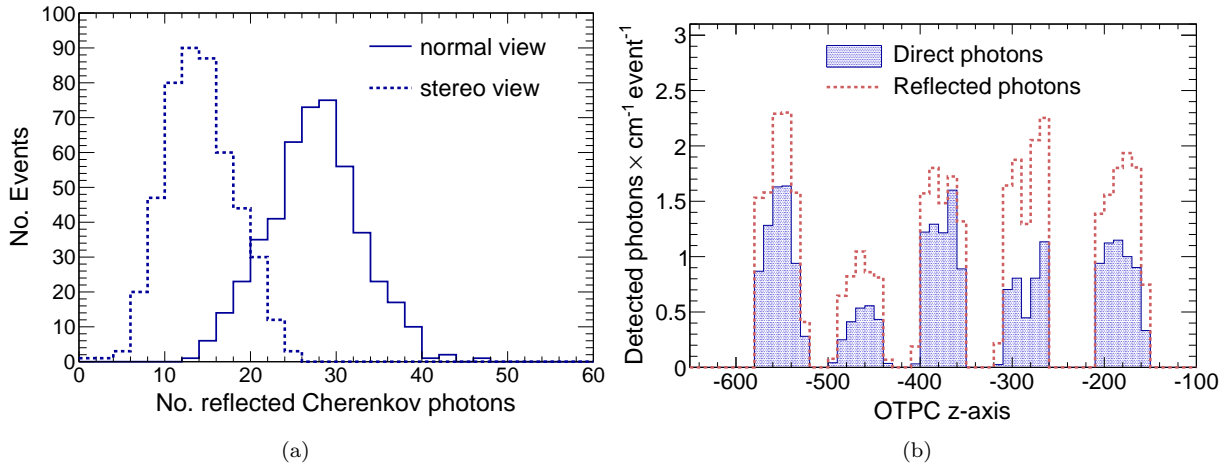


Figure 29: (a) Number of reflected Cherenkov photons per event. The direct and mirror-reflected photons are separated by applying a time-cut to the data presented in Fig. 23. The number of direct photons per event is shown in Fig. 26a. (b) Number of direct and reflected photons detected per event per cm. The five discrete distributions along the OTPC z-axis are the 5 PM locations (left to right, PM 0 to 4).

13. Spatial resolution

To fully reconstruct charged particle tracks, the mirror-reflected photons are used in combination with the direct Cherenkov light. A second time cut is made on the data in the rotated time basis, t' (Fig. 23), to isolate the reflected Cherenkov photons. A normal view time-cut of >2.05 ns and a stereo view time-cut of >2.0 ns were used on the data. A time-gap of 100 ps between the direct and reflected photon time-cuts was used to separate the two regions.

The number of reflected photons per event in the normal and stereo views is shown in Figure 29a. The relative number of direct and reflected detected photons at each PM per event per cm is shown in Fig. 29b. As expected from Fig. 23, there is a preponderance of reflected over direct photons.

A straight-forward way to reconstruct the spatial position of the trajectory is to take the difference of the mean direct photon arrival times and the mean reflected photon arrival times in the t' basis. Explicitly, the time difference at a PM for a given event a , Δt_{PM} , using this method is

$$\Delta t_{PM} = \frac{1}{n} \sum_{i=1}^n t'_i{}^{mirror} - \frac{1}{m} \sum_{j=1}^m t'_j{}^{direct} - t_0 \quad (9)$$

where n is the number of reflected photons per event per PM and m is the number of direct photons per event per PM. A time reference for the event, t_0 (the R_2 trigger signal time), is subtracted from each event for alignment. This time-difference measurement is inserted into Eqn. 6 to obtain the lateral displacement of the particle track.

The result of Equation 9 is shown in Figure 30 when grouping together the normal view data and stereo view data separately. This result incorporates the same 522 events used in the measurement shown in Fig. 27. The normal view has an average time difference of 810 ± 59 ps; the stereo data show a time difference of

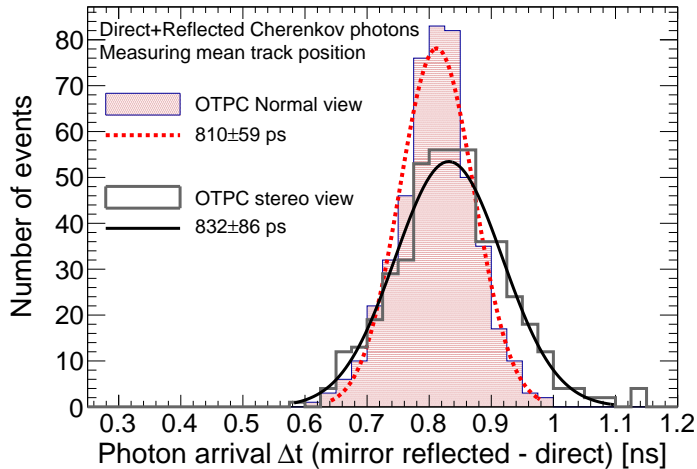


Figure 30: Time-of-arrival difference between the direct and mirror reflected Cherenkov photons for the normal and stereo views. The time differences were measured using Eqn. 9. The normal view has an average time difference of 810 ± 59 ps and the stereo data shows a time difference of 832 ± 86 ps.

832 ± 86 ps⁴. These 1σ uncertainties correspond to spatial resolutions of 9.6 mm and 13.9 mm, respectively, when combining data from the PMs.

To utilize the OTPC as a tracking detector, we use each PM to resolve the spatial coordinates along the z - and ϕ -axes. We require that an event has more than three direct and three mirror-reflected photons for each PM. There are 127 through-going events that satisfy this condition. As expressed in Eqns. 9, the radial position, r , along the z and ϕ axes of the OTPC is defined as the displacement from the nominal beam axis. Using Eqns. 9 and 6 we can reconstruct r at each of the five PM positions in z - and ϕ . The five distributions in the radial position are shown in Figure 31.

The properties of the data in Figure 31 are shown in Table 3. The reconstructed radial position, r , at each z position is consistent with $r=0$, which is the expectation with the through-going trigger. At each normal view PM, the resolution is about 15 mm on this measurement. On the stereo view, the average error is 17.5 mm. We expect the beam spatial location to have an RMS variation of ~ 7 mm from the measured beam output position in the R_2 trigger (Fig. 10).

Figure 32 shows the 3D track reconstruction of the event displayed in Figs. 19a and 24. The direct Cherenkov photons are projected onto the reconstructed radial position, r , and the OTPC normal and stereo-view coordinates are decomposed into the Cartesian coordinate system defined in Fig. 2.

14. Conclusions

We have constructed and characterized the performance of a small prototype optical-TPC (OTPC), in which we measured the time and position of arrival for each individual photon emitted by Cherenkov radiation from a charged particle traversing the water volume. The photon arrival times and 2D spatial

⁴The mean time differences are slightly larger than measured on the full 16 GeV/c dataset (§11.1 and Fig. 23) due to the event selection and the time cuts applied to separate the direct and mirror-reflected photons described in the text

Table 3: Average reconstructed radial positions of tracks along OTPC z-axis. The OTPC center-line is defined as $r=0$. These data are shown in Figure 31

PM	\bar{z} [mm]	ϕ [radians]	reconstructed r [mm]
0	-550	0.567	-1.5 ± 15.6
2	-375	0.567	-2.75 ± 14.8
4	-185	0.567	-4.62 ± 15.6
1	-460	-0.567	0.7 ± 19.8
3	-290	-0.567	2.2 ± 16.4

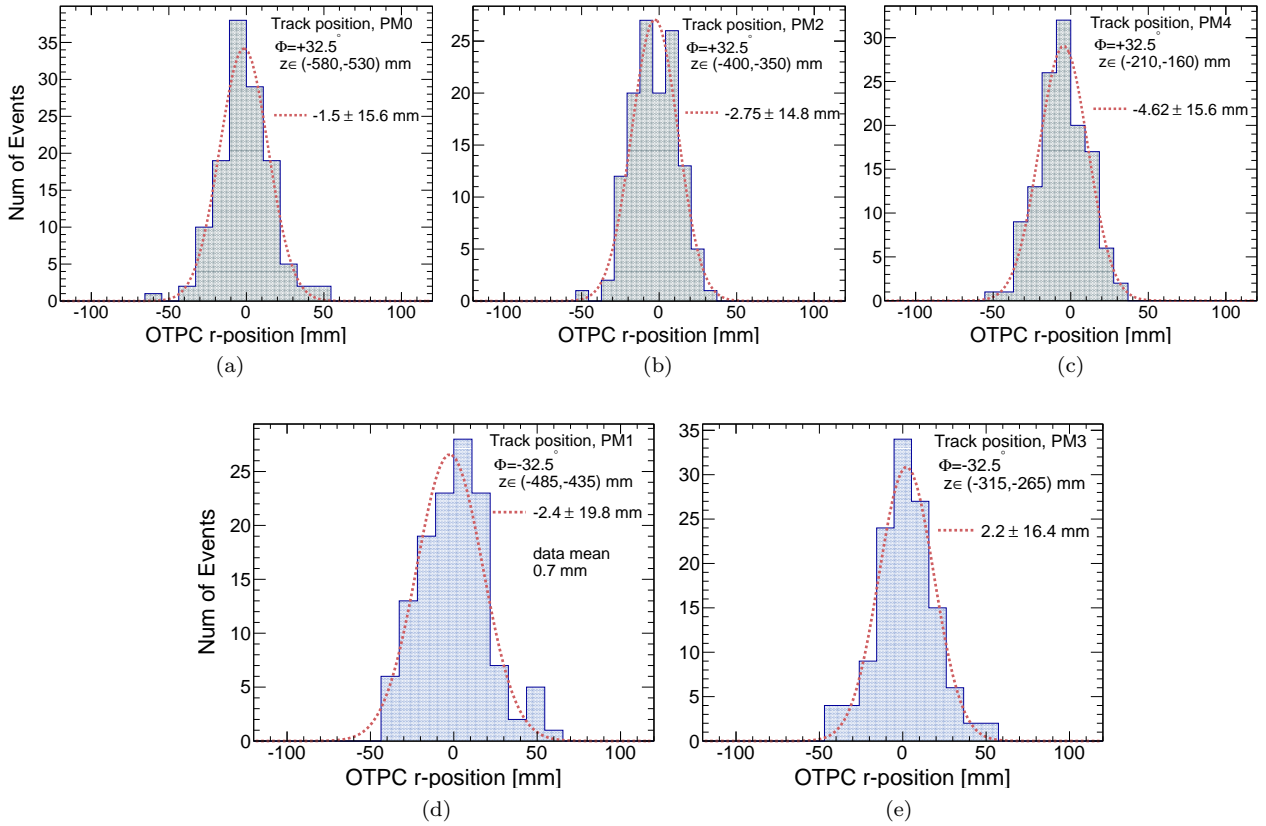
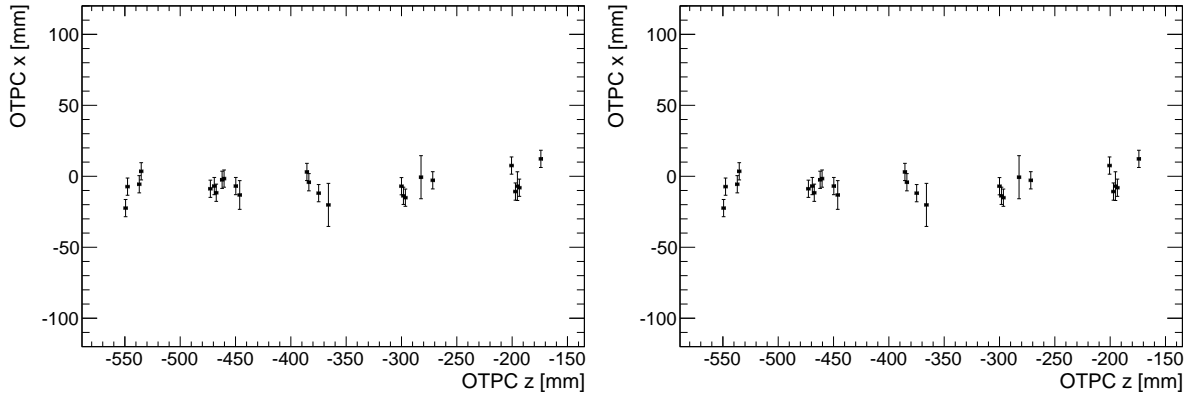
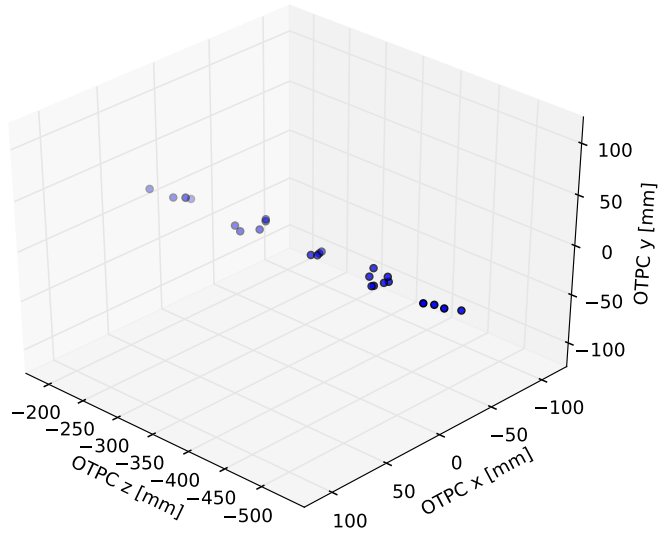


Figure 31: The reconstructed radial track position along the OTPC z-axis at each PM ϕ -location.



(a)

(b)



(c)

Figure 32: The 3D track reconstruction of the event shown in Figures 19a and 24. The rotated times, t'_i , of the direct Cherenkov photons are projected on the reconstructed radial position (stereo, normal, z) and decomposed into Cartesian (x,y,z) coordinates. (a) The track x vs. z position. (b) The track y vs. z position (c) The reconstructed x, y, and z of the track.

locations are resolved to ~ 75 ps and $\leq 3 \times 3$ mm², respectively, using the digitized waveforms. Given the arrival positions and the drift times, the particle track position and direction can be reconstructed.

While the present prototype is small and still primitive, several of the techniques developed here may scale to much large detectors capable of reconstructing events and vertices in more complicated event topologies such as would be expected in proton decay, neutrino-less beta decay, and neutrino interactions [32, 33, 34].

The ability of the OTPC to resolve time differences much smaller than 1 nanosecond lends itself to two strategies relevant to the economics of scale-up for larger detectors. The first was to cheaply multiply the $\sim 7\%$ photocathode coverage on the surface of the detector by using optical mirrors; the mirrors more than doubled the OTPC light collection. For each track, the mirrors allowed for the added collection of Cherenkov photons impinging on the detector wall opposing the MCP-PMT. The reflected photons are clearly time-resolved in the data with an average delay of 770 ps compared to the direct Cherenkov light. The second strategy is to digitize the microstrips at one end of the strip with the opposing end open, so that direct pulse and the reflection from the far end provides two distinct \sim ns-wide pulses per detected photon. This cuts the electronics channel count in half, and has the added advantage that the times-of-arrival at each end are measured on the same electronics channel.

For through-going tracks recorded at a secondary beam momentum of 16 GeV/c, we observed 80 ± 20 detected Cherenkov photons per event. Each photon is resolved in time, z , and ϕ , allowing a view of the 3D trajectory. We measured an angular resolution, assuming a straight track, of 60 mrad when fitting events in which more than 8 direct photons were detected among the three MCP-PMTs in the OTPC normal view. By time-resolving the direct and mirror reflected photons at 60 ps, we measure a transverse resolution on the particle track of 15 mm. We note that an entire reconstructed event takes place over a 40-cm track length and in a duration of less than 3000 picoseconds.

15. Acknowledgements

We thank the staff of the Enrico Fermi Institute Electronics Development Group for their essential technical and intellectual contributions, in particular Mircea Bogdan for the design of the Central DAQ printed-circuit card, Fukun Tang for first suggesting the use of high-bandwidth microstrips for the photodetector anodes, Mark Zaskowski for electronics assembly, and Mary Heintz for her superb support of the infrastructure for electronics design, computing, and web documentation. We are indebted to Richard Northrop and Robert Metz, both of the University of Chicago Physical Sciences Division Engineering Center, for expertise in mechanical design and skilled machining, respectively, and Justin Jureller of the UC Materials Research Science Center for providing his time and the expertise to make the OTPC water-absorbance measurements.

We express our gratitude to Jeffrey DeFazio, Raquel Ortega, and Emile Schyns of PHOTONIS, Inc., for providing technical details and support for the Planacon photodetectors. We thank Howard Nicholson, then of the DOE, for suggesting the use of LAPPDs for neutrino physics and for the name of the Optical Time Projection Chamber.

This work could not have been done without the support of Fermilab and, in particular, the Fermilab Test Beam operations group: Eugene Schmidt Jr., Erik Ramberg, Mandy Rominsky, and Aria Soha. Todd Nebel and Greg Sellberg provided excellent mechanical support. The LArIAT collaboration provided technical assistance and knowledge in welcoming the OTPC operation parasitically in their beam line.

This work was supported by National Science Foundation grant PHY-1066014 and Department of Energy award DE-SC0008172. Part of this work was performed at the Fermilab Test Beam Facility, which is

operated by Fermi Research Alliance, LLC under Contract No. De-AC02-07CH11359 with the United States Department of Energy.

References

- [1] J. Beringer, et al. (PDG). Review of Particle Physics - Passage of particles through matter. *Phys. Rev. D*, 86:323–338, 2012.
- [2] B.W. Adams, A. Elagin, H.J. Frisch, R. Obaid, E. Oberla, A. Vostrikov, R.G. Wagner, J. Wang, and M. Wetstein. Timing characteristics of large area picosecond photodetectors. *Nucl.Instr.Meth A*, 795:1–11, 2015.
- [3] J. Milnes and J. Howorth. Picosecond time response characteristics of micro-channel plate PMT detectors. *SPIE USE*, 8:89–100, 2004.
- [4] O.H.W. Siegmund, A.S. Tremsin, J.V. Vallerga, R. Abiad, and J. Hull. High resolution cross strip anodes for photon counting detectors. *Nucl.Instr.Meth A*, 504:177–181, 2003.
- [5] N. Kishimoto, M. Nagamine, K. Inami, Y. Enari, and T. Ohshima. Lifetime of MCP-PMT. *Nucl.Instr.Meth A*, 564:204–211, 2006.
- [6] F. Tang, et al. Transmission-line readout with good time and space resolutions for Planacon MCP-PMTs. In *Topical Workshop on Electronics for Particle Physics, CERN 2008*, pages 579–583, 2008.
- [7] H. Grabas, H.J. Frisch, E. Oberla, J.-F. Genat, R. Northrop, D. McGinnis, B. Adams, M. Wetstein, R. Obaid, and F. Tang. RF Strip-Line Anodes for Psec Large-Area MCP-based Photodetectors. *Nucl.Instr.Meth A*, 711:123–131, 2013.
- [8] B.W. Adams, A. Elagin, H.J. Frisch, R. Obaid, E. Oberla, A. Vostrikov, R.G. Wagner, and M. Wetstein. Measurements of the gain, time resolution, and spatial resolution of a 20×20 cm² MCP-based Picosecond Photo-Detector. *Nucl.Instr.Meth A*, 732:392, 2013.
- [9] E. Oberla, H. Grabas, J.-F. Genat, H.J. Frisch, K. Nishimura, and G. Varner. A 15 GSa/s, 1.5 GHz bandwidth waveform digitizing ASIC. *Nucl.Instr.Meth A*, 735:452–461, 2014.
- [10] LAPPD collaboration, website: <http://psec.uchicago.edu>.
- [11] B.W. Adams, M. Chollet, A. Elagin, R. Obaid, E. Oberla, A. Vostrikov, M. Wetstein, and P. Webster. A test-facility for large-area microchannel plate detector assemblies using a pulsed sub-picosecond laser. *Rev. Sci. Instrum.*, 84, 2013.
- [12] PHOTONIS USA Pennsylvania, Inc. Planacon XP85022 32×32 datasheet, Jan 2014. <http://www.photonisusa.com>.
- [13] Porter Pipe & Supply Co., website: <http://www.porterpipe.com>.
- [14] Optical data from: (1) Enhanced Aluminum 4-6 λ First-Surface Mirror, Edmunds Optics (2) Fused-silica glass port www.mcmaster.com (3) Optical coupling gel, code 0607, Cargille Labs. Spray paint used for light absorbing surfaces: Rust-oleum, textured, indoor/outdoor, black.
- [15] A Cary 8500 dual-beam spectrophotometer was used for this measurement.
- [16] S. Dazeley and M. Yeh. Personal communication, 2015.
- [17] S. Seibert and A. LaTorre. Fast Optical Monte Carlo Simulation With Surface-Based Geometries Using *Chroma*. <http://chroma.bitbucket.org/>, 2011.
- [18] J.D. Jackson. *Classical Electrodynamics*. John Wiley & Sons, Inc., 3rd edition, 1999.
- [19] I. Tamm and I. Frank. *Compt. Rend. Acad. Sci USSR*, 14:109, 1937.
- [20] M. Daimon and A. Masumura. Measurement of the refractive index of distilled water from the near-infrared region to the ultraviolet region. *Appl. Opt.*, 46:3811–3820, 2007.
- [21] P. Russer. *Electromagnetics, Microwave Circuit, And Antenna Design for Communications Engineering*. Artech House, 2nd edition, 2006. Chapter 7, Transmission-Lines and Waveguides.
- [22] Samtec, Inc. 34 AWG Micro Coax Cable Datasheet, May 2015.
- [23] A Texas Instruments Clock Generator/Jitter Cleaner was used, model no. CDCE62005, and configured such that a 40MHz clock was distributed to each PSEC4 chip using LVCMOS signaling.
- [24] G.S. Varner, L.L. Ruckman, J.W. Nam, R.J. Nichol, J. Cao, P.W. Gorham, and M. Wilcox. The Large Analog Bandwidth Recorder and Digitizer With Ordered Readout (LABRADOR) ASIC. *Nucl.Instr.Meth A*, 583:447–460, 2007.
- [25] K. Nishimura and A. Romero-Wolf. A Correlation-Based Timing Calibration & Diagnostic Technique for Fast Digitization ASICs. *Physics Procedia*, 37:1707–1714, 2012.
- [26] D. Stricker-Shaver, S. Ritt, and B.J. Pichler. Novel calibration method for switched capacitor arrays enables time measurements with sub-picosecond resolution. *Nuclear Science, IEEE Transactions on*, 61(6):3607–3617, Dec 2014.
- [27] Fermilab Test-Beam Facility. <http://ppd.fnal.gov/ftbf/>.
- [28] F. Cavanna et al. LArIAT: Liquid Argon In A Testbeam. arXiv:1406.5560, 2014.

- [29] T.J. Roberts and D.M. Kaplan. G4beamline simulation program for matter-dominated beamlines. In *Particle Accelerator Conference, 2007. PAC. IEEE*, pages 3468–3470, 2007.
- [30] E. Oberla. *Charged particle tracking in a water Cherenkov optical time-projection chamber*. PhD thesis, University of Chicago, 2015.
- [31] Advanced Laser Diode Systems. Picosecond Diode Laser - PiLas Manual and Test Report, Jun 2013.
- [32] G. Orebi Gann et al. Advanced Scintillator Detector Concept (ASDC): A Concept Paper on the Physics Potential of Water-Based Liquid Scintillator. arxiv:1409.5864, 2014.
- [33] M.C. Sanchez, M. Wetstein, et al. Letter of Intent: The Accelerator Neutrino Neutron Interaction Experiment (ANNIE). arXiv:1504.0180, 2015.
- [34] C. Aberle, A. Elagin, H.J. Frisch, M. Wetstein, and L. Winslow. Measuring directionality in double-beta decay and neutrino interactions with kiloton-scale scintillation detectors. *Journal of Instrumentation*, 9(06):P06012, 2014.